TEKTONIKA

How Fast Can Minibasins Translate Down a Slope? Observations from 2D Numerical Models

Naiara Fernandez [*1,2], **Oliver B. Duffy** [2], **Christopher A-L. Jackson** [3,4], **Boris J.P. Kaus** [5], **Tim Dooley** [2], **Michael Hudec** [2]

[1]GFZ German Research Centre for Geosciences, Telegrafenberg, 14473, Potsdam, Germany | [2]Bureau of Economic Geology, Jackson School of Geosciences, The University of Texas at Austin, University Station, Box X, Austin, Texas, 78713-8924, USA | [3]Basins Research Group (BRG), Department of Earth Science & Engineering, Imperial College, Prince Consort Road, London, United Kingdom, SW7 2BP, UK | [4]Jacobs, 5 First Street, Manchester, M15 4GU, UK | [5]Institute of Geosciences, Johannes Gutenberg University Mainz, J.-J.-Becher-Weg 21, D-55128 Mainz, Germany

Abstract Minibasins are important features in salt-bearing basins and are abundant in salt-detached continental slopes where the salt and the overlying sedimentary cover (including minibasins) undergo seaward translation due to gravity. One question which is relevant for understanding the structural evolution of salt-detached slopes is what controls the translation velocity of the salt layer and of overlying minibasins. The aim of this study is three-fold: 1) to compare minibasin downslope translation velocity with salt translation velocity; 2) to understand what controls minibasin translation velocity and 3) to understand how minibasins translating at different velocities can kinematically interact and modify strain patterns around them. To address these questions, we present a 2D numerical modelling study. In addition to parameters that control salt velocity, we show that minibasin thickness is the main factor controlling minibasin velocity in the numerical models. If the minibasin is far from the base-of-salt, its velocity can be estimated by a 1D analytical solution of salt flowing on a slope. Specifically, thicker minibasins translate slower than thinner minibasins. If the minibasin is close to the base-of-salt, viscous drag slows it further, and the numerical results deviate from the 1D analytical solution. Finally, we assess how several minibasins of differing thicknesses and translation velocities, may diverge or converge as they translate downslope, resulting in varying strain patterns around them. Findings from our numerical modelling provide additional conceptual understanding of structural evolution of salt-detached continental slopes that have significant implications for understanding minibasin behaviour, and interpreting strain patterns around them.

Executive Editor:
Craig Magee
Associate Editors:
L. Muniz Pichel
C. Salazar-Mora
Technical Editor:
Aline Ribeiro
Mohamed Gouiza

Reviewers:
Attila Balazs
Conor O'Sullivan
Dan Tamas

Submitted:
27 October 2022
Accepted:
22 September 2023
Published:
28 November 2023

1 Introduction

Minibasins are important features of many salt-bearing basins. They are small synkinematic basins that form by subsidence into a relatively thick layer of salt (*Jackson and Talbot*, 1991). Minibasins can form in different geodynamic settings (e.g. rift basins, foreland basins) and many are found on salt-detached slopes formed along continental margins (e.g. *Jackson and Hudec*, 2017). One characteristic of salt-detached slopes is the seaward translation of the salt and its overlying sedimentary cover. Over geological time scales, salt behaves as a viscous fluid. As a result, on salt-bearing continental slopes, salt moves downslope due to gravity in response to two main driving mechanisms: gravity spreading (deformation and collapse of a rock mass by its own weight) and gravity gliding (downslope translation of the rock mass over an inclined detachment) (e.g. *De Jong and Scholten*, 1973; *Ramberg*, 1981; *Brun and Merle*, 1985). Distinguishing between these mechanisms on natural continental slopes is difficult, given it is likely that both processes contribute to the downslope flow of salt (e.g. *Schultz-Ela*, 2001; *Rowan et al.*, 2004; *Brun and Fort*, 2011, 2012; *Peel*, 2014; *Ge et al.*, 2019a,b). In both cases, as salt flows downslope the capping sedimentary cover on top also translates. One of the main outcomes of this style of salt-related deformation is the partitioning of continental slopes into three different domains: an up-dip extensional domain and a down-dip compressional domain, separated by a translational domain (Figure 1a and b).

We know that gravity causes salt (and overlying sedimentary cover) to flow down a slope, but how fast does salt move? Direct observation of salt flow is restricted to areas where salt is exposed at the Earth's surface, such as in Iran, where aerial extrusions from salt diapirs form salt glaciers (e.g. *Lees*, 1927; *Kent*, 1958; *Wenkert*, 1979). These well-exposed salt structures have enabled direct measurements of lateral salt flow at observational time scales (i.e.,

*✉ naiara@gfz-potsdam.de

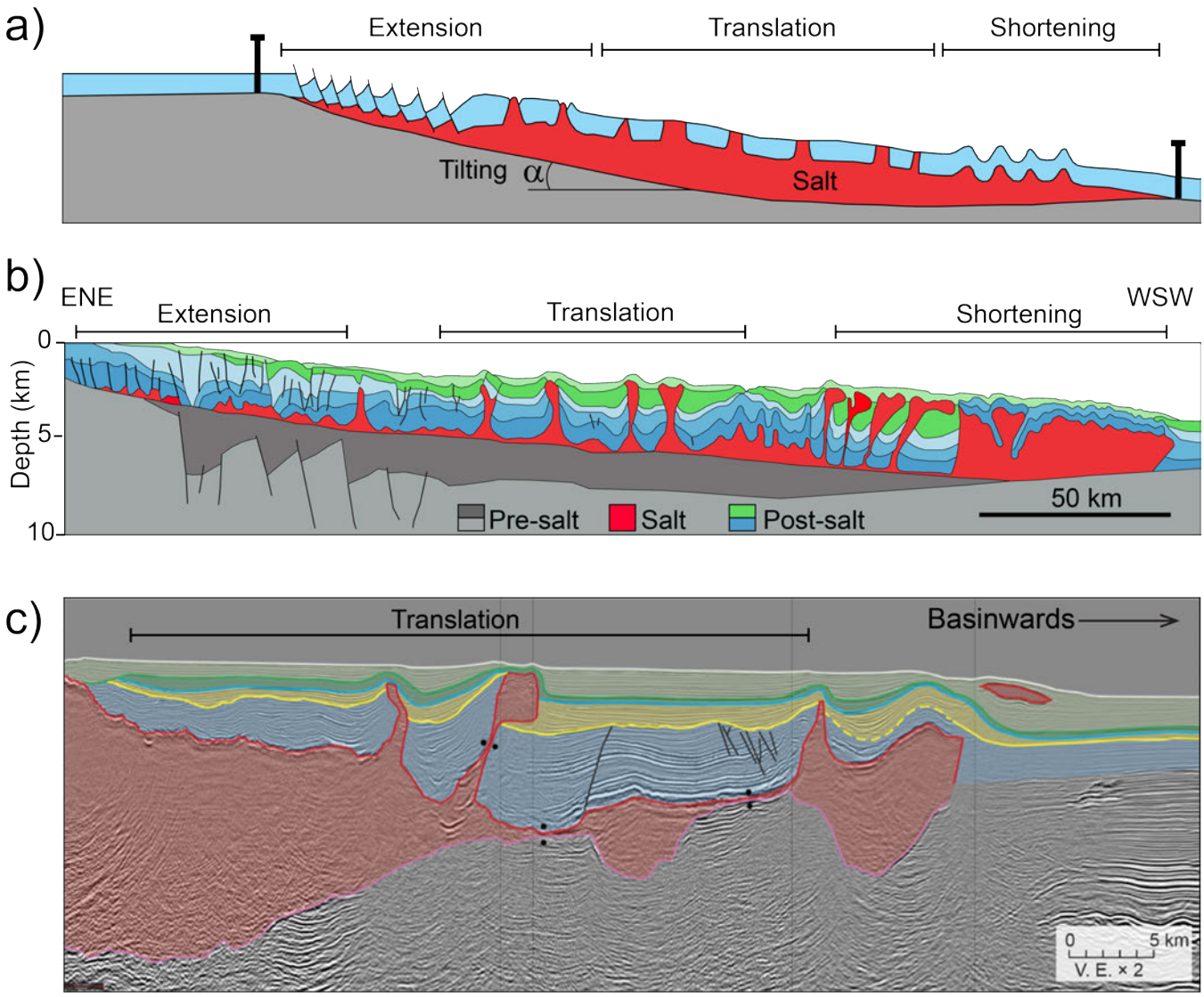

Figure 1 – **a)** Schematic model of a salt-detached slope system with extension-translation-shortening structural zonation. The translational domain is populated with minibasins that translate on top of the salt, as the salt moves downslope. **b)** Regional interpreted seismic cross section along the Lower Congo Basin (modified from *Marton et al.*, 2000) with characteristic downdip shortening domain and updip extension domain. The mid-slope translational zone is characterized by the presence of minibasins and vertical diapirs. **c)** Seismic cross section of the Northern Gulf of Mexico, where minibasins of different thicknesses can be observed. These minibasins are, at present day, close to the lower portion of the slope and the thickest one is welded at its base. However, these minibasin of different thicknesses were initiated and originated at a position further up the slope from their present-day position. Seismic section is shown with permission from WesternGeco.

days to years), using, for example, geomorphological observations and surveys (*Wenkert*, 1979; *Talbot and Rogers*, 1980; *Talbot and Jarvis*, 1984; *Talbot et al.*, 2000). In more recent years, satellite based interferometric synthetic aperture radar (InSAR) time series analysis has provided further insights into the salt uplift and lateral flow rate in some of these well-exposed salt structures (e.g. *Aftabi et al.*, 2010; *Ghassemi and Roustaei*, 2021; *Mohammadnia et al.*, 2021; *Zhang et al.*, 2021). Lateral salt displacement values reported in such studies range from <1 to 400 cm/yr. However, subaerial salt flow responds to complex dissolution-precipitation processes that change the rheology of the salt, which means short-term salt flow rates cannot be directly extrapolated to salt flow over geological time scales (10^3-10^6 years) (e.g. *Urai et al.*, 2008; *Zhang et al.*, 2021). In addition, salt extrusion associated with the Iranian salt diapirs is driven by tectonic shortening, which directly impacts and controls the rate of salt extrusion and lateral flow. Thus, our understanding of the rate of gravity driven salt flow at geological time scale and at regional scale (i.e. continental slope scale) remains poor.

In the case of salt-detached slopes, the velocity of salt flow in the geological past can be estimated by indirect observations. For example, in the northern Gulf of Mexico salt canopy, estimation of salt velocities comes from the analysis of seismic reflection data. More specifically, this technique requires the assessment of age-constrained stratigraphic cut-offs at the base-of-salt over which the salt was advancing at the same time new sediments were being deposited in front of the

advancing salt (e.g. *Tauvers*, 1993). Advance rates of salt sheets using structural restorations of geological sections constructed from seismic interpretations provide long-term advance or flow rates of 0.1-2 cm/yr (e.g. *Diegel et al.*, 1995; *Peel et al.*, 1995; *Schuster et al.*, 1995; *Jackson and Hudec*, 2017, and references therein). More recently in the Levant Basin (Eastern Mediterranean), fluid escape pipes transecting the mobile salt layer have been used to estimate an average salt velocity of 0.2 cm/yr for a period of 1.7 Myr (*Cartwright et al.*, 2018). These attempts to constrain salt flow at geological time scale, based on natural examples, provide values that are 2-3 orders of magnitude slower than the ones directly measured in subaerial salt glaciers.

If constraining how fast salt moves at geological time scale (thousands to millions of years) is challenging and has many uncertainties, constraining the translation velocity of the sedimentary cover that overlies salt is even more so. Compared to the up-dip extensional and the down-dip compressional domains, clear indicators of displacement magnitudes (e.g. fault cutoffs) are usually absent in the translational domain (e.g. *Jackson and Hudec*, 2005). This is even more true if instead of a continuous cover, the translational domain is populated with minibasins that are only partially interconnected, as is the case of minibasin provinces located in continental slopes (e.g. Lower Congo Basin, Figure 1b; Northern Gulf of Mexico; Figure 1c). It is not unusual for velocity estimates of the sedimentary cover in the translational domain to be inferred from observations of salt-detached ramp syncline basins and/or rafted minibasins (e.g. *Jackson and Hudec*, 2005; *Jackson et al.*, 2010; *Fiduk*, 2014; *Pilcher et al.*, 2014; *Pichel et al.*, 2018, 2020; *Evans et al.*, 2021; *Evans and Jackson*, 2021; *Fernandez et al.*, 2021). Estimates of the translation rate of sedimentary cover based on reconstructed cross-sections provide velocities in the ranges of 0.1-4 cm/yr (e.g. rafted minibasins in the Gulf of Mexico and ramp synclines in eastern Mediterranean *Jackson et al.*, 2010; *Evans et al.*, 2021; *Evans and Jackson*, 2021, respectively). However, minibasin translation velocities are presumably the result of the lateral salt flow in which they are transported and their own vertical subsidence into salt. It is also presumed that minibasin translation rates will dramatically decrease as they are close to welding at their base (e.g. *Wagner and Jackson*, 2011). Furthermore, the downslope translation of minibasins can be obstructed by base-salt relief or friction associated with primary welding, processes that result in locally complex strain patterns of the sedimentary cover (e.g. *Krueger*, 2010; *Duffy et al.*, 2020). Further complications arise from the fact that coevally subsiding minibasins can mutually alter their subsidence patterns and rates (e.g. *Fernandez et al.*, 2019), potentially also affecting their translation velocities.

One question that has not been explicitly addressed before is: how different is the velocity of downslope-flowing salt from the velocities of overlying minibasins? More specifically, do minibasins translate at different velocities? If so, does minibasin thickness, geometry and density affect how fast they translate before they weld? Understanding if, why, and how salt and minibasins move at different velocities is relevant for understanding the structural evolution of salt-detached slopes. Ultimately, the absolute distance a minibasin can travel on a slope is constrained by its maximum translation velocity, as well as the time over which the translation could occur. Thus, having a better understanding of what controls minibasin translation velocity will help constrain structural restorations of salt basins. Furthermore, if minibasins translating at different velocities coexist on a slope, this can result in differential translation between minibasins and may help explain the complex strain patterns around minibasins that are characteristics of some salt-detached slopes (e.g. *Krueger*, 2010; *Duffy et al.*, 2020; *Fernandez et al.*, 2021).

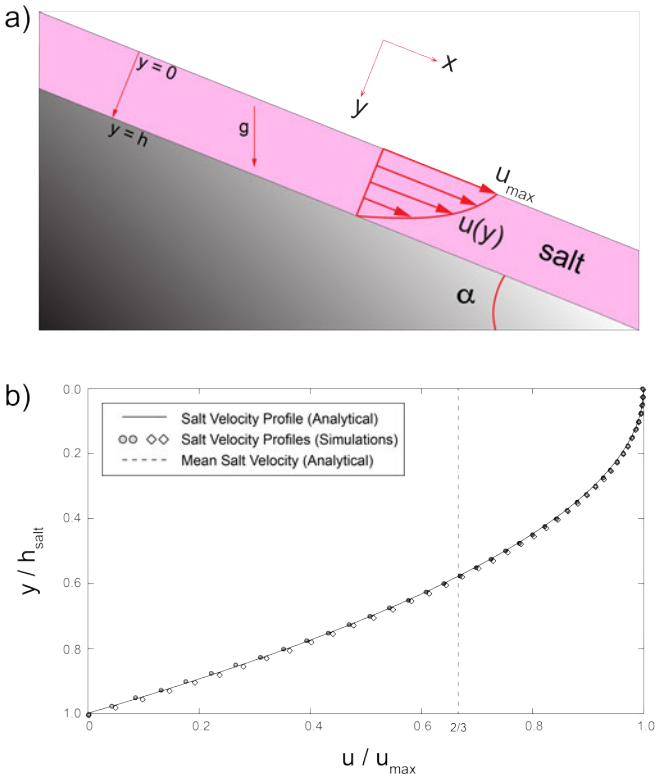

Figure 2 – **a)** Schematic cartoon of a linear viscous salt layer on an inclined plane. The analytical solution assumes that the thickness of the salt layer remains constant. The base of the salt layer has a no-slip boundary condition and the top is a free-stress surface. An analytical expression for the resulting velocity (u) profile can be obtained for the given assumptions. See text for details. **b)** Comparison between the normalized velocity profile calculated from the analytical expression (continuous line) and the velocities extracted from two different numerical simulations (circles and diamonds). The differences between the numerical and analytical solutions are within 1%.

The aim of this study is thus three-fold: 1) to compare minibasin downslope translation velocity with salt translation velocity; 2) to understand what controls minibasin translation velocity; and 3) to understand how minibasins translating at different velocities can kinematically interact and modify strain patterns on the slope. To achieve this goal, we undertake 2D numerical modelling consisting of three simulation series. In the first series, we model a simple scenario where, as a result of gravity, a constant-thickness salt layer moves downslope on an inclined plane (Figure 2a). This scenario reflects a simplification of the translational domain of a salt-detached continental slope (Figure 1a). For this particular scenario, an analytical solution already exists (e.g. *Turcotte and Schubert*, 2002), which we use to benchmark our numerical models. In the second series, we use the same model geometry as in the first (i.e. constant thickness salt layer over an inclined plane), but we add a single, isolated minibasin at the up-dip portion of the slope. Different minibasin thicknesses, widths and densities are then tested, replicating how in natural salt basins, minibasin size (thickness and width) and sedimentary fill (density as a proxy of lithology) vary as a function of their maturity, their structural position, and/or the overall regional geological setting in which they form and evolve. Given that minibasins are rarely found in isolation, in the third simulation series, we add an array of three minibasins in the up-dip portion of the slope, and we assess how they interact as they translate downslope. The goal of this study is not to model a specific natural example. Rather, our objective is to identify the key principles and controls of salt flow and minibasin translation velocities at geological time scale on salt-detached slopes. The values given are not intended to be taken as absolute values of velocity, but instead to provide a self-consistent framework to understand the relative impact of different parameters (e.g., slope angle, salt thickness, minibasin thickness and minibasin density) in minibasin translation velocity. However, when appropriate, comparisons with velocities reported in natural examples in the literature are provided throughout the text.

2 Analytical Solution of Salt Flowing Down a Slope

We are first interested in understanding regional-scale salt flow on salt-detached slopes. We can consider the salt-detached slope as equivalent to an inclined plane overlain by a viscous fluid layer of constant thickness (e.g. *Turcotte and Schubert*, 2002). The inclined plane would be analogous to the slope, and the viscous layer would be analogous to the salt (Figures 1 and 2a). A schematic diagram of the setup is shown in Figure 2a.

Using a fluid dynamics approach, the velocity profile of the unidirectional flow of a viscous fluid down an inclined plane can be obtained assuming the following conditions: the flow occurs in a layer of constant-thickness (h) viscous fluid; no-slip condition ($u = 0$) at $y = h$; and free-surface ($\tau = 0$) condition at $y = 0$.

$$u = \frac{\rho g \sin\alpha}{2\mu}\left(h^2 - y^2\right) \tag{1}$$

The equation can be solved for the maximum and mean velocity in the layer, obtaining:

$$u_{max} = \frac{\rho g \sin\alpha}{2\mu}\left(h^2\right) \tag{2}$$

$$u_{mean} = \bar{u} = \frac{\rho g \sin\alpha}{3\mu}\left(h^2\right) \tag{3}$$

where, u is velocity, ρ is salt density, μ is salt viscosity, g is gravity, α is the slope angle and h is the salt layer thickness. Derivations of equations (1), (2), and (3) are described in the Supporting Information. These equations can be used to calculate both the maximum and mean velocity of the salt on a salt-detached slope, if we use the appropriate values for the parameters (within the ranges observed in the natural examples described above). A normalized analytical velocity profile can be obtained from Eq. (1) by plotting it in the non-dimensional y/h and u/umax axes (Figure 2b). The maximum velocity occurs at the surface of the salt, where y = 0 and the velocity is zero at y = h (Figure 2b). The average value of the salt velocity profile corresponds to $u_{mean} = \frac{2}{3}u_{max}$. Eq. (1) is also used to perform calculations for a combination of the main parameters: salt thickness and slope angle. We use a range of salt thicknesses (0.1-4 km) and slope angles (0.1-4°) that covers ranges comparable to those encountered on natural salt-detached continental slopes (e.g. *Peel*, 2014, and references therein). Salt density is taken to be 2200 kg/m^3, an appropriate value for a halite salt-rock with 5% of impurities (e.g. *Gevantman and Lorenz*, 1981; *Jackson and Hudec*, 2017). The rheology of salt at geological time scale is still widely debated and depends on many factors, including the tectonic setting (e.g. *Urai et al.*, 2008; *Jackson and Hudec*, 2017). While a non-linear rheology of salt has been argued for a tectonically inactive setting without salt flow (e.g. *Li et al.*, 2012), recent numerical models have argued in favour of a linear-viscous rheology of salt in extensional settings (*Granado et al.*, 2021). In this study, we model the salt as a linear-viscous material characterised by a viscosity of 10^{18} Pa s (estimates of 10^{17} – 10^{21} Pa s are found in the literature; *Mukherjee et al.*, 2010, and references therein). Assuming a linear-viscous rheology of the salt is a simplification that facilitates comparison with the simple analytical solution outlined above. The mean and maximum salt velocities calculated analytically for the given parameter ranges are plotted in Figure 3 (maximum velocity contours represented by solid lines, mean velocity contours by dashed lines). For example, for

a salt layer of 2 km thickness, with a slope angle of $\alpha = 2°$ (grey circle, Figure 3), the maximum salt velocity is 4.75 cm/yr and the mean salt velocity is 3.17 cm/yr. The analytical results illustrate that salt flows faster with increasing slope angle and increasing salt thickness (see Eqs. 2 and 3 and Figure 3).

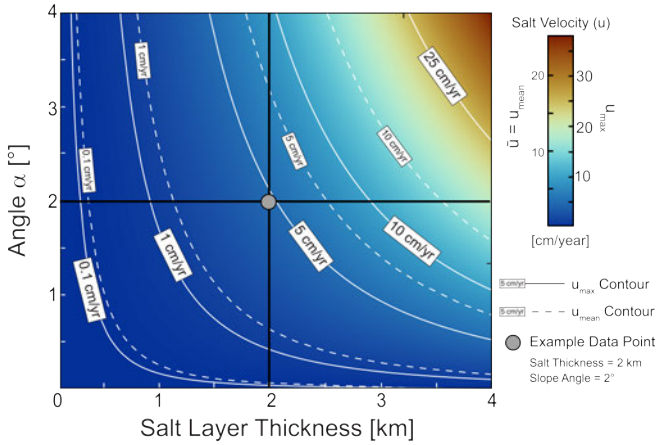

Figure 3 – a) Plot of the maximum velocity (u_{max}) and mean velocity (u_{mean}) of the salt layer moving down an inclined plane for a combination of inclination angles and thicknesses of the salt layer. The maximum velocity is located at the top of the salt layer. The circle represents the combination of parameters discussed in the text and used in most of the simulations.

3 Numerical Modelling Approach

The analytical solution serves as a benchmark for our numerical experiments (see below). We use the 2D finite-element code MVEP2 (*Kaus*, 2010; *Thielmann and Kaus*, 2012; *Johnson et al.*, 2014). MVEP2 solves the equations of conservation of mass and momentum for incompressible materials with visco-elasto-plastic rheologies, and employs Matlab-based MILAMIN approach (*Dabrowski et al.*, 2008) for efficiency. The code uses a Lagrangian approach, where material properties are tracked by randomly distributed markers that are advected according to the velocity field that is calculated in a deformable numerical grid. Remeshing of the grid is performed every time step. The method and numerical implementation are explained in detail in *Kaus* (2010).

The numerical model domain is a 120 km-long and 10 km-high modelling box (Figure 4a). All the boundary conditions of the modelling box are set to free-slip (velocity is parallel to the boundary). The initial geometry within the model box consists of an inclined basement capped by an undeformed salt layer of constant thickness (Figure 4a). The top of salt is modelled as an internal free surface along which relief can develop. In numerical simulations with this initial geometry, salt will immediately flow downslope due to gravity, causing salt to thicken at the base of the slope, and thin at the upper slope (Figure 4b). To keep the thickness of salt constant, an internal boundary condition has been applied to the interface between the salt and the air/water (Figure 4c and d). The aim of the internal boundary condition is to 'remove' salt flowing above the initial inclined topography at the base of the slope, and 'add' salt to fill in the area at the top of the slope depleted of salt below the initial topographic level (Figure 4d). This boundary condition ultimately produces a continuous flow of salt on the slope, keeping the salt thickness constant such that it is comparable to the scenario for which the analytical solution exists (compare Figure 2a and Figure 4c). The variables tested in these numerical simulations are the following: inclination of the slope (α), salt viscosity (μ) and density (ρ) and thickness of salt layer (h). The results of numerical experiments are compared with the predictions of the analytical solution to test the appropriateness of the numerical simulations (Figure 2b). Velocity profiles obtained from numerical simulations with constant salt thickness plot on top of, or very close to, the velocity profile obtained analytically (Figure 2b). With a resolution of 1000 x 100 element nodes (element size of 120 m x 100 m), the deviance of the numerical solution from the analytical solution is ~1%.

The central portion of the slope in the numerical simulations (between -40 km to 40 km) has a salt velocity profile that remains constant through time, not influenced by edge or boundary effects resulting from the applied internal boundary condition (Figure 4c). Thus, we consider this portion of the numerical domain to be an appropriate representation of an ideal translational domain of a continental slope (Figure 1a). In such an idealized domain, the effects of the up-dip extensional and down-dip compressional domains are far enough away as not to affect the dynamics of salt flow and translation (Figure 4c). Herein, we will focus on the central portion of the slope.

4 How Fast do Minibasins Translate Downslope?

The series of numerical simulations described in this section are aimed at understanding what controls the downslope translation velocities of minibasins on a salt-detached slope. The geometry of the numerical models is the same as the one used to reproduce the analytical solution of salt flowing on an inclined plane (Figure 3a). However, in this series a single isolated minibasin is added to the upper slope in each of the simulations. Although minibasins are rarely isolated in nature, these simulations aim to develop an understanding of the fundamental controls on minibasin downslope translation, in the absence of neighbouring minibasins. It is also important to note that the minibasins used in the simulations approximate rounded-at-the-base semi-circles to minimize the effect of the basal viscous drag, whose effect is discussed later. Two model sub-series are described in this section: 1) one in which the density of the minibasins is equal

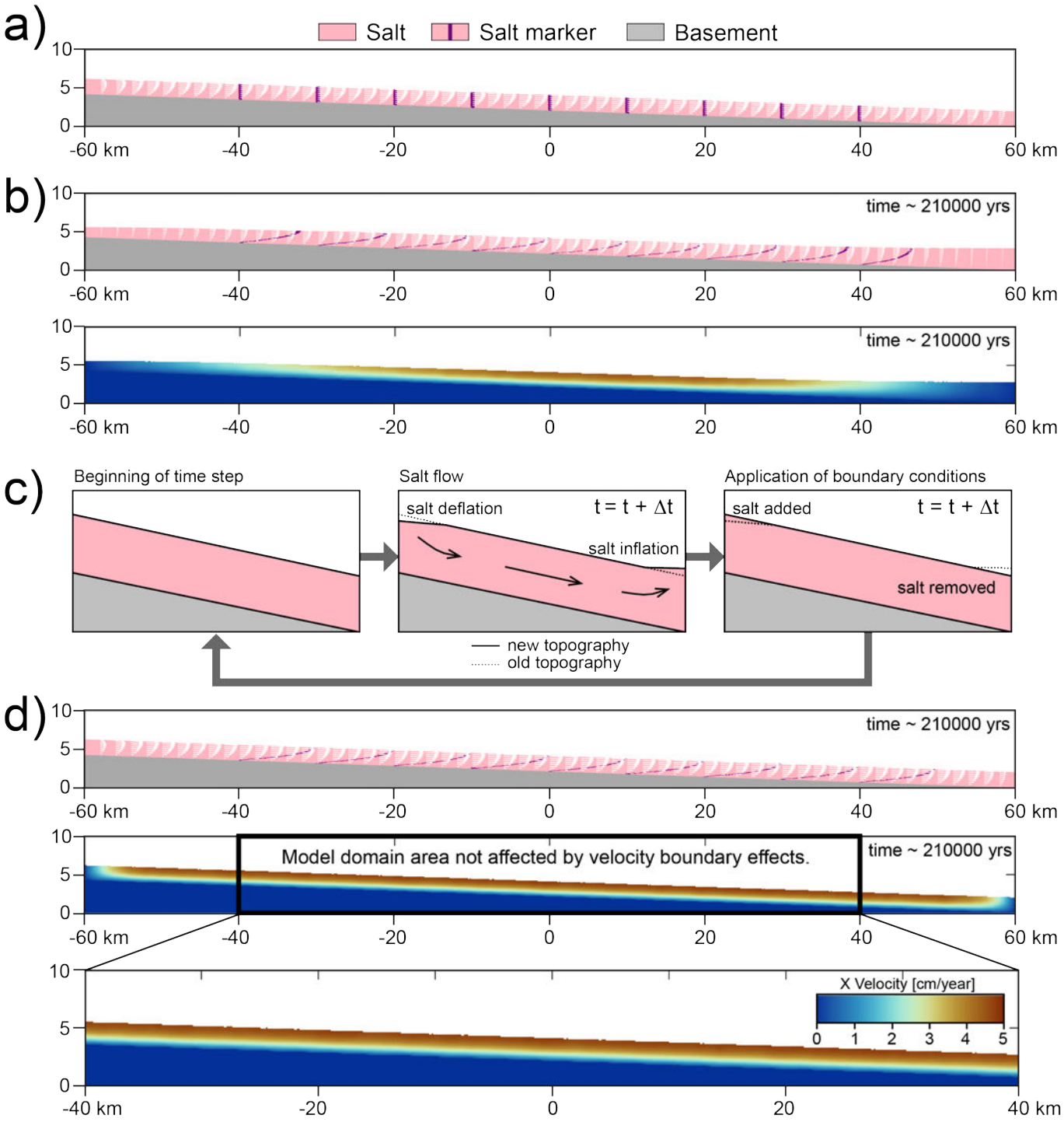

Figure 4 – a) Example of an initial model geometry. The modelling box is 120 km x 10 km in size. It contains an inclined basement with a constant thickness layer of salt on top. In this example, the slope angle is α= 2° and salt thickness (H) is 2 km. **b)** Intermediate result (geometry in the upper panel and X velocity in the lower panel) of a numerical simulation where the salt is allowed to flow and develop topography. Starting geometry of the numerical simulation is shown in (a). Note the salt deflation at the updip portion of the slope and the salt inflation at the downdip portion of the slope and the extent of the maximum X velocity area localized in the central portion of the slope. **c)** Schematic cartoon (not to scale) illustrating the implementation of the internal boundary condition to keep the salt layer thickness constant. The sketched stages are repeated every time step in the numerical simulations. **d)** Intermediate result of a numerical simulation where the salt thickness is kept constant, by applying an internal boundary conditions as sketched in (c). Note the more homogeneous X velocity profile across the slope compared to (b). The portion of the slope between -40 km and 40 km, is considered to be homogenous and not influenced by edge effects.

to that of the salt (i.e. neutral-buoyancy minibasins); the aim of this sub-series is to understand the effect of minibasin geometry (mainly thickness and width) on their translation velocity; and 2) one in which the minibasin density differs from the salt, such that the minibasin either subsides (i.e. minibasins are denser than salt) or rises (i.e. minibasins are less dense than salt) as it translates downslope.

We have performed simulations with a salt viscosity (μ_{salt}) of 10^{18} Pa s, a salt density (ρ_{salt}) of 2200 kg/m^3, slope angles (α) of 2-4°, and a salt thickness (H_{salt}) of 2-4 km. However, we only describe here the results of simulations with a slope angle of 2° and a salt thickness of 2 km, values that are within the range of those reported for different natural examples of salt-detached slopes (results of simulations with a slope angle of $\alpha = 2°$ and H_{salt} = 4 km are provided in Supporting Information). The minibasins in the numerical simulations are modelled as being visco-plastic following the Drucker-Prager yield criterion. The minibasins are characterized by a friction angle (ϕ) of 30°, and a cohesion (C) of 20 MPa, relatively competent material, to avoid internal deformation as they translate. Simulations are run for several hundreds of time-steps. The last time-steps are discarded and are not described here, because as the minibasins approach the base of the slope they get closer to the area where the effects of the applied internal boundary conditions influence the salt velocity. For each of the simulations the velocity field calculated in the code is used to extract the translation velocity of the minibasin at each time-step. Next, we describe the observations from each model sub-series.

4.1 Models with Neutral-Buoyancy Minibasins

In models containing neutral buoyancy minibasins ($\rho_{minibasin}$ = ρ_{salt} = 2200 kg/m^3), minibasins translate downslope with the flowing salt. As the density of the minibasins is equal to that of the salt, they do not subside into or rise above salt (Figure 5, also Figure SI-1 in Supporting Information). After around 1,000,000 years, the minibasins have traversed the central portion of the slope (Figure 5).

We now explore the effect of minibasin thicknesses. The initial thickness of the minibasins considered is either 900 m (herein referred to as 'thin' minibasin) or 1250 m (herein referred to as 'thick' minibasin). These values correspond to minibasin thickness (T_{mb}) to salt thickness (H_{salt}) ratios of T_{mb}/H_{salt} ~0.425 and 0.625, which represent minibasins at two different growth stages (between their initiation as thin depocenters, to their maximum thickness-to-salt ratio of T_{mb}/H_{salt} = 1, once they weld). When different minibasin thickness-to-salt thickness ratios are used, we specify it in the text. Images of the simulations are shown for the initial geometry and for two time-steps, after ~500,000 and ~1,000,000 years, along with their corresponding velocity plots (Figure 5a, b). Our results show that the thin minibasin translated further downslope than the thick minibasin during the same time interval (compare Figure 5a and b). The translation velocity of neutral buoyancy minibasins remains nearly constant throughout the simulation (Figure 5c, d). The mean velocity of the minibasins during this translational stage is 3.52 cm/yr and 4.09 cm/yr, for the thick and thin minibasins, respectively (Figure 5c, d). Thicker minibasins translate at lower velocities. When compared to the velocity obtained for salt (i.e. 4.75 cm/yr maximum salt velocity; 3.17 cm/yr mean salt velocity), we note that minibasins translate at a velocity lower than the theoretical maximum salt velocity (Eq. (2)). However, whereas the thick minibasin translates at a velocity lower than the theoretical mean salt velocity (Eq. (3)), the thin minibasin translates faster than the theoretical mean salt velocity.

The effect of the free surface that allows for the build-up of salt topography in the central part of the models is best noticed in a simulation with thicker salt (4 km) and slope angle of 2° (Figure SI-2). In this case, the shallowest and fastest moving salt, extrudes onto the up-dip side of the minibasin.

4.2 Models with Subsiding and Buoyant Minibasins

In models where minibasins have a density different to that of the salt, they will either subside into salt (if denser than salt) or rise buoyantly (if less dense than salt) as they translate downslope. A snapshot after the same time interval in simulations with subsiding and buoyant thick and thin minibasins is shown in Figure 6 (also Figure SI-3). The minibasins in Figure 6 have density values of $\rho_{minibasin}$ = 2000, 2100, 2200 2300, 2400, and 2500 kg/m^3 (salt density being ρ_{salt} = 2200 kg/m^3). Our models show that, unsurprisingly, the denser the minibasin, the faster it subsides into salt. In our simulations, sediment fills the accommodation created as a minibasin subsides. Accommodation in downslope-translating minibasins is invariably created on the up-dip side of the minibasin. By the end of the simulation, the minibasins are overlain by a wedge-shaped sediment package that thickens up-dip (light brown colour wedge shapes seen in Figure 6). The systematic up-dip orientation of the wedge-shaped sediment package arises from the simple geometry of the model setup, where single, isolated minibasins are subsiding into salt flowing down a smooth base of salt. The denser the minibasin is initially, the thicker the final wedge-shaped package is at the end of the simulation (Figure 6). When the results of simulations with minibasins of different densities are compared at the same time step, it can be observed that the amount of distance travelled by the minibasins differs (Figure 6). The denser the minibasin, the shorter its translation distance (Figure 6). As expected from the experiment with neutral-density minibasins of the previous section, the thinner minibasins, which in this case are the less dense ones, translated further.

We can further assess the effect of density on minibasin translation velocity by looking at temporal changes in velocity (Figure 7, also Figure SI-4). This shows that subsiding minibasins tend to decrease their translation velocity as they subside and become thicker (Figure 7). Conversely, buoyant minibasins tend to increase their velocity through time as they

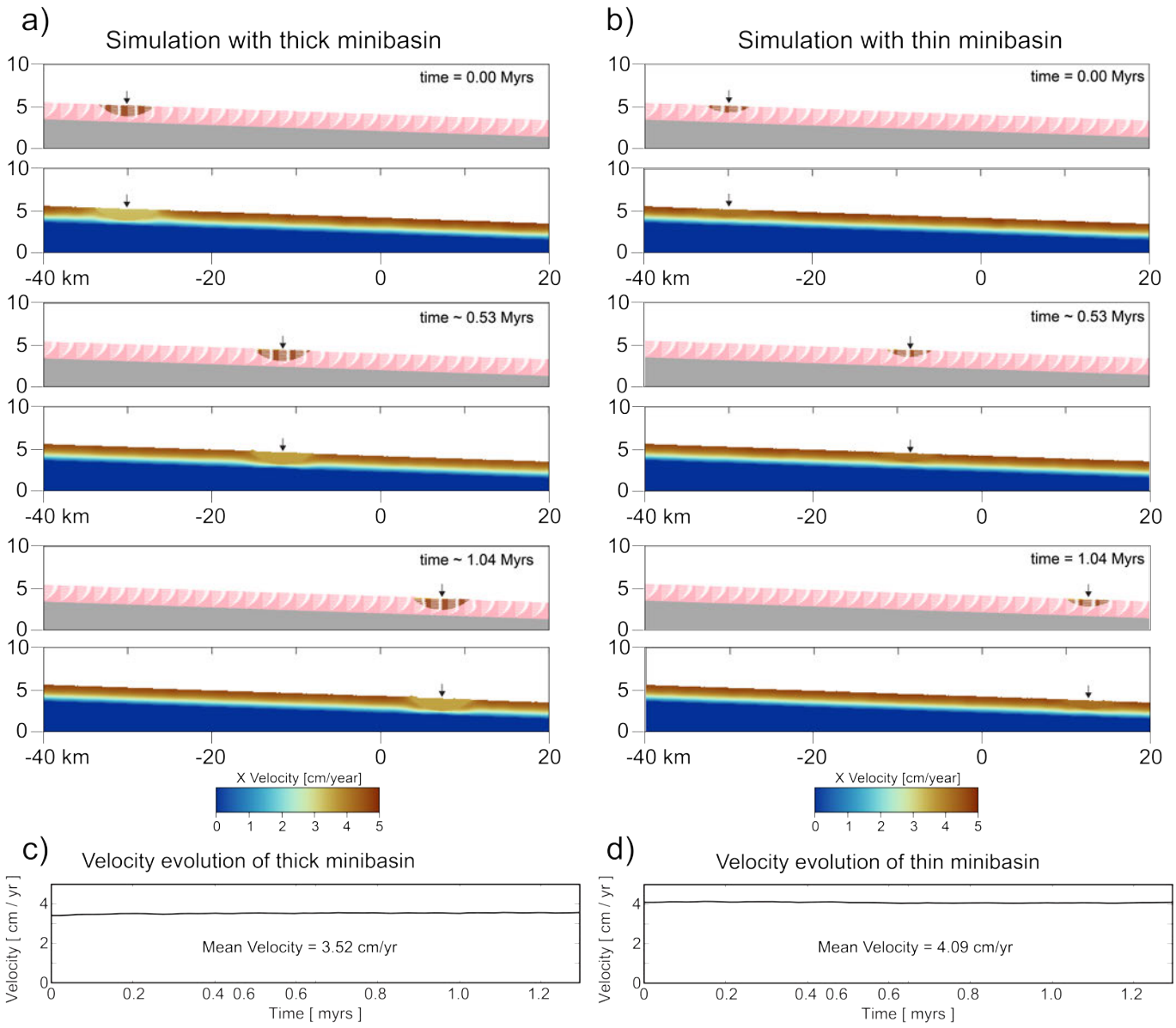

Figure 5 – **a)** and **b)** Geometry of basement (grey colour), salt (pink colour) and minibasin (brown and orange colours) and velocity field of three different time steps of two numerical simulations. Black arrows indicate the position of minibasins. **a)** Simulation with a thick minibasin. **b)** Simulation with thin minibasin. **c)** and **d)** Graphs with the evolution through time of the mean velocity of the minibasin from the simulations. **c)** Simulation with thick minibasin. **d)** Simulation with thin minibasin. Note that the thin minibasin has higher velocity through time (b and d) and thus, higher mean velocity than the thick minibasin (a and b). The higher velocity of the thin minibasin results in the thin minibasin moving further downslope than the thick minibasin in the screenshots shown in (a) and (b).

rise over salt (Figure 7). However, the temporal increase of translation velocity in buoyant minibasins is small compared to the velocity decrease through time associated with subsiding minibasins (Figure 7).

5 What Controls Minibasin Velocity?

As minibasins in the simulations are embedded in the flowing salt, the first-order control on minibasin velocity in the absence of any other external factor (i.e. tectonics) is presumably the velocity of the flowing salt. A theoretical salt velocity profile, and its corresponding maximum and mean salt velocities can be calculated from the analytical solution (Eqs. (1), (2), (3); Figure 2 and Supporting Information). However, that analytical solution is a 1D channel flow approximation, where there is no shear stress variation in the direction parallel to the slope (see Appendix for details). Given this constraint, we now discuss how the thickness (normalized over salt thickness) and aspect ratio of minibasins affect their translation velocity, and how this relates to the analytically predicted salt velocity.

The sketch in Figure 8 illustrates a constant thickness salt layer on a slope with a minibasin embedded in the salt. The thickness of the minibasins at its centre is T_{mb}, thus, the basal position of the minibasin in a y-axis profile would correspond to $y = T_{mb}$. This position ($y = T_{mb}$) can be used

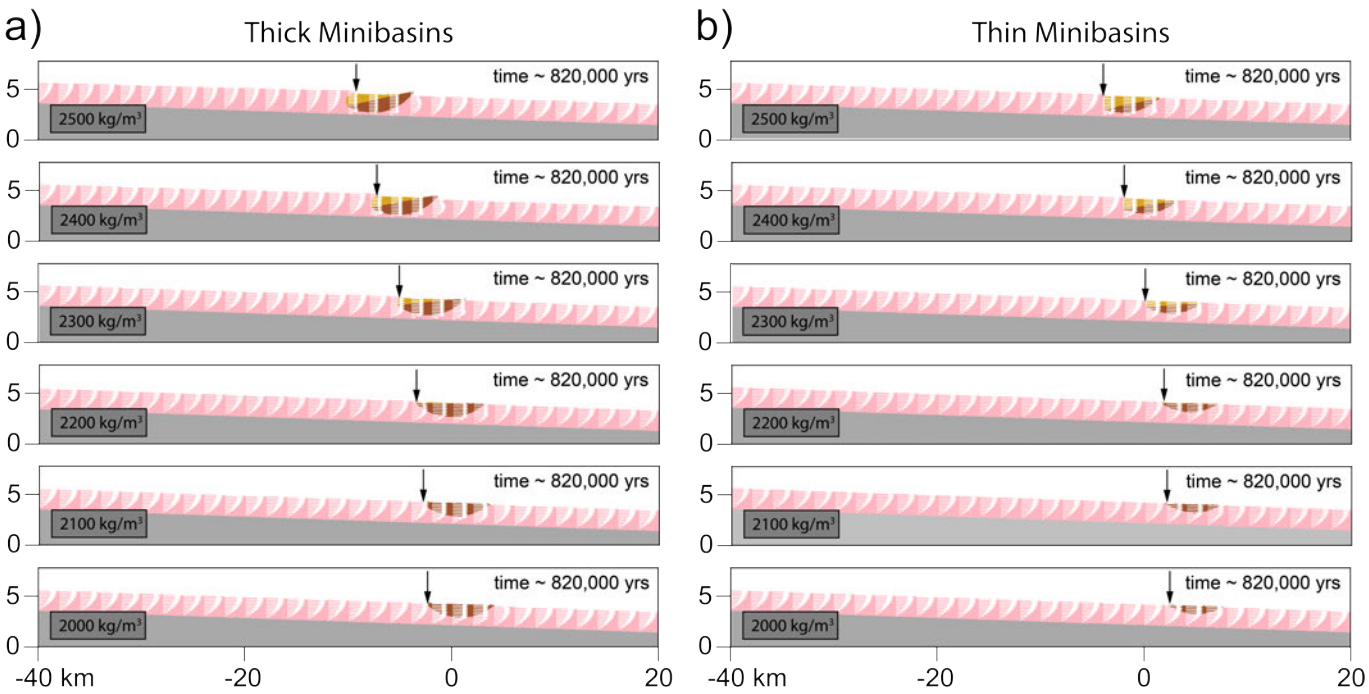

Figure 6 – a) and **b)** Screenshots at the same final time step (time ~820,000 yr) of numerical simulations with thick (a) and thin (b) minibasins of different densities. Black arrows indicate the position of the minibasins. The amount of minibasin translation varies according to their densities. Upper panels show the highest density minibasins (denser than salt; 2500, 2400 and 2300 kg/m^3) and have the least amount of translation (a, b). Highest minibasin translation is seen at the lower panel (lowest density minibasin, less dense than salt; 2100 and 2000 kg/m^3). Minibasins that are denser than salt subside as they translate downslope, allowing for sediment accumulation in their up-slope edge, in the form of a synkinematic sediment wedge (orange colour). The accumulation of new sediment results in an increase of minibasin thickness through time.

to conceptually divide the salt layer profile into two different portions: an upper salt portion, from 0 to y = T_{mb}, and a lower salt portion, from y = T_{mb} to y = h. Various theoretical salt velocity profiles (and corresponding maximum and mean values) can be calculated considering the salt layer to be split into two portions at y = T_{mb}. The theoretical profiles are illustrated in Figure 8 (also Figure SI-A9 in Supporting Information).

The analytical salt profile described by Eq. (1) can be used to calculate the theoretical salt velocity profile for the complete salt layer (thickness h). Then, the mean salt velocity of the upper portion of this entire salt velocity profile can be calculated and we will refer to this mean velocity as, $\bar{u}_{mb}$. Similarly, Eq. (1), can be used to obtain the mean velocity of a theoretical salt velocity profile of the upper salt portion (h' = y = T_{mb}). We refer to this mean velocity as $\bar{u}_{h'=y}$. The corresponding mathematical expressions of these definitions are described in detail in the Appendix. Next, we compare the results from the numerical simulations of minibasin translation, with these analytically-predicted, mean velocity profiles.

5.1 Minibasin Thickness

Numerical simulations with neutral buoyancy minibasins of different thicknesses have been used to extract the minibasin velocity after the initial time-step, for three different initial model geometries (H = 4 km and α = 4°; H = 4 km and α = 2°; H = 2 km and α = 4°). Given that we have already demonstrated that the velocity of neutral buoyancy minibasins in the numerical models is approximately constant through time (see Figure 5), we have taken the value of one time-step in each simulation. Each numerical model result is plotted in Figure 9a. Numerically calculated velocities of neutral buoyancy minibasins for minibasin whose thickness is < ~70% of the total salt thickness closely fall on the analytically calculated line described by the following equation (check Supporting Information for details):

$$u_{mb} = \frac{\rho g h^2 \sin\alpha}{2\mu} - \frac{\rho g y^2 \sin\alpha}{3\mu} \quad (4)$$

The minibasin velocity can be captured by the above equation, which is based on a 1D analytical solution of salt flowing on a slope. Minibasin velocity is proportional to the velocity of an upper salt sublayer with thickness equivalent to the minibasin thickness (see Supporting Information). It must be noted that minibasin velocity calculated from the numerical models deviates from the line described by Eq. (4) when the minibasin thickness approximates the salt thickness (i.e. minibasin thickness T_{mb} > ~70% H or T_{mb}/H_{salt} > ~0.7; Figure 9a). This implies that in the numerical models there is an effect of the base salt boundary on minibasin translation, which is not captured by the simple 1D analytical solution of Eq. (4). For cases of Tmb/Hsalt < ~0.7, there is enough distance between the base-of-minibasin

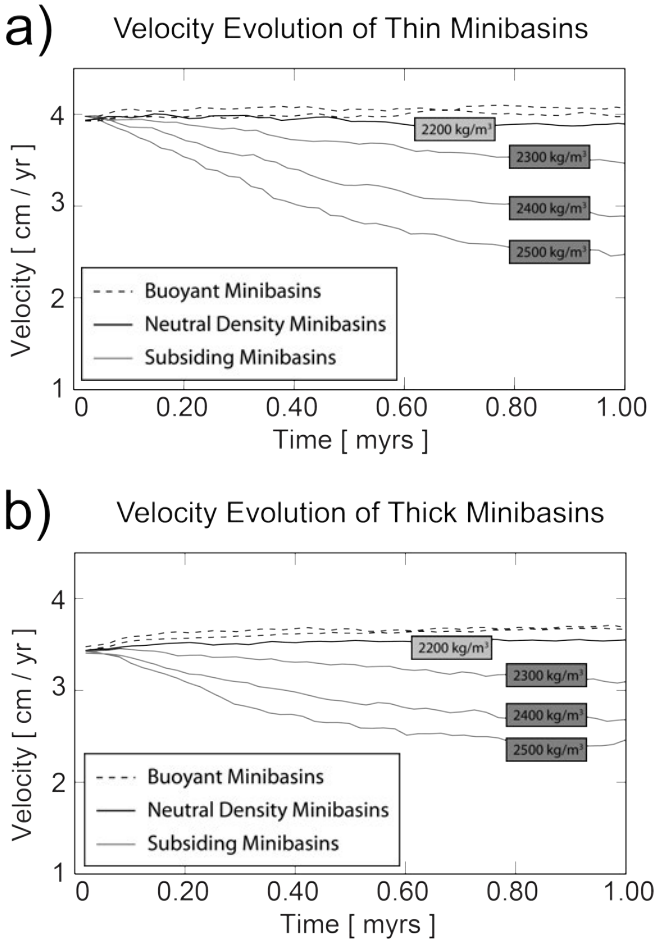

Figure 7 – Graphs showing the velocity evolution in simulations with minibasins whose density is different than that of the salt. **a)** Simulations with thick minibasins. **b)** Simulations with thin minibasins. Note that, when minibasins are denser than the salt, the velocity of the minibasins tend to decrease through time. Also, the higher the density the faster the decrease in the velocity it is. The opposite is true for minibasins that are less dense than salt, which increase their velocity through time.

and base-of-salt so that salt can still flow below the minibasin at a rate at which the salt velocity profiles both sides (up-dip and down-dip) of the minibasin are similar, and equivalent to the sum of velocities of the minibasin and of the salt below the minibasin. Hence, a simple 1D analytical solution of salt flowing on a slope broadly captures the dynamics of the entire slope, including the minibasin translation velocity. For cases of T_{mb}/H_{salt} > ~0.7, the effect of the proximity of the minibasin to the base-of-salt is to increase the viscous drag between the base-of-minibasin and base-of-salt (e.g. *Wagner and Jackson*, 2011). This increased basal viscous drag implies that salt flow below the minibasin is not sufficient to maintain similar salt velocity profiles on both sides of the minibasin. As a result, salt accumulates up-dip of the minibasin and is drained down-dip, meaning the minibasin velocity cannot be captured by a simple 1D analytical solution of salt flowing on a slope.

Compared to neutral-density minibasins, we

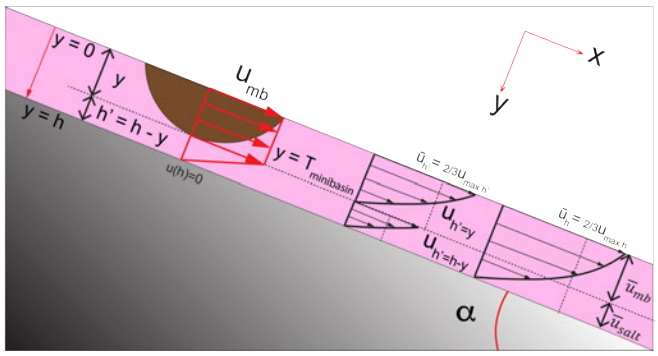

Figure 8 – Sketch of a layer of salt on a slope, with a minibasin on it. The position at y that corresponds to the minibasin thickness $y=T_{mb}$ is used to split the salt layer into two portions: upper salt, $h'=y=T_{mb}$ and lower salt, $h'=h-y$. The velocity profile that would correspond to each portion is shown, together with the theoretical salt velocity profile corresponding to the complete salt layer thickness h. The maximum and mean velocities described in the text are illustrated here. $\bar{u}_{mb}$ corresponds to the mean velocity calculated from the upper portion of the velocity profile, that overlaps with the minibasin thickness. $\bar{u}_{salt}$ corresponds to the mean velocity calculated from the lower portion of the velocity profile that is below the minibasin. Both mean velocities can be obtained by integrating the velocity profile for the corresponding portions.

have seen that subsiding minibasins increase their thickness and decrease their translation velocity through time. We have plotted the evolution of thickness and corresponding minibasins velocity in numerical simulations with subsiding minibasins, for minibasins with a density = 2500 kg/m^3 (Figure 9b). The results of three numerical simulations with different initial minibasin thickness to salt thickness ratios of T_{mb}/H_{salt} ~0.325, 0.575 and 0.825 are shown in Figure 9b. Subsiding minibasins follow the analytical curve described by Eq. (4) as they increase their thickness. However, as for the neutral minibasins, the effect of the model base (base-of-salt) is to dramatically decrease minibasin translation velocity (Figure 9b). This more pronounced decrease in minibasin translation velocity occurs when subsiding minibasins reach a thickness that is close to that of the salt layer (>70%), at which point the model results deviate from the analytical solution of Eq. (4) (Figure 9b).

The graphs of Figure 9, can be used in conjunction with Eq. (1), to predict the minibasin velocities that would be expected in the numerical models, without actually performing new simulations. For a given minibasin thickness (normalized over salt thickness), from the graphs of Figure 9, we can obtain the minibasin velocity (normalized over maximum analytical salt velocity). That normalized minibasin velocity can be converted to an "actual" velocity (e.g. cm/yr) by using the analytical maximum salt velocity as calculated from Eq. (1). However, it must be noted that in the analytical solution and the numerical simulations discussed in the text, the top of salt is modelled as a subaerial free-surface. A salt-detached

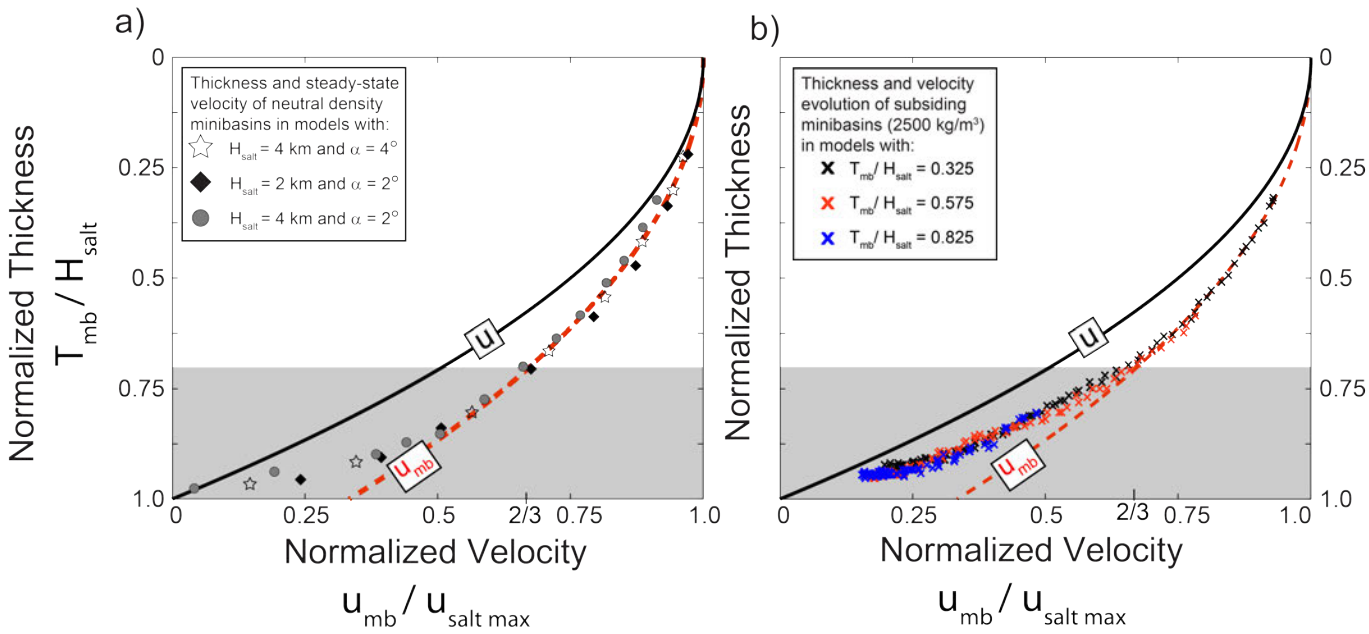

Figure 9 – a) Normalized velocity profiles (x axis = u/u_{max}; y axis = y/h) calculated with the analytical solution and equations Eq. 1 (black line), 4 (red line) and 5 (blue line), and the various averaged profiles described in the text (dashed lines). Each of the markers (circles, starts, diamonds) correspond to one numerical simulation with neutral-density minibasins of different initial thickness. Three sets of parameters were used in the numerical simulations of neutral-density minibasins (each set represented by one type of marker, star, circle or diamond). As noted in the text, neutral-density minibasins maintain their translation velocity through time, so for each simulation, the minibasin velocity of a single (initial) time step is plotted in the normalized graph. Overall, the minibasin velocity of the numerical models fall in a curve that relates the salt velocity at the base of the minibasin, and the mean velocity of the portion corresponding to the minibasin thickness (red dashed line). Only, when the initial minibasin thickness is close to the thickness of the salt layer (T_{mb} > 0.7h; greyed area), the velocity is lower than predicted by the curve, and the results plot in a different trend in the graph. **b)** Normalized velocity profiles (same as in a). Markers (crosses) indicate the minibasin velocity and thickness evolution through time of three simulations in which the minibasin is denser than salt, and thus subsiding. The velocity of subsiding minibasins decreases through time, as they subside and become thicker (see text for details). Overall the velocity and thickness evolution of subsiding minibasins follow a trajectory as described by the analytical curve (red dashed line), until they reach a certain thickness (shaded grey). When the minibasin thickness is closer to the salt thickness (and close to the base-of-salt), the minibasin translation velocity decreases more dramatically.

slope that is completely under water, is subjected to the additional load imposed by the water column, with the load increasing with salt depth downslope. The salt velocity in a slope covered with water would therefore be lower than for a subaerial slope, the effective difference between the velocities depending on the water column difference across the slope, which is related to the slope angle and slope length. We have checked the differences with a numerical simulation. For the example given earlier in Section 2 of a 2° slope and 2 km thickness salt, the mean salt velocity is 3.17 cm/year in a subaerial slope. Instead, if the model domain is assumed to be filled with water of density 1000 kg/m^3 with depth increasing from 0 up-dip to 4.2 km down-dip, the resulting mean velocity of salt due to gravity-driven flow is 2.49 cm/yr. It is for this reason that minibasin velocities provided in the graphs of Figure 9 are normalized to the maximum salt velocity. The velocity of salt in a water covered slope depends on more parameters (mainly model domain length) that are not considered here for simplification but that may be worth exploring in the future.

5.2 Minibasin Aspect Ratio

As mentioned previously, the minibasins used in the simulations in Figures 5 and 6 are approximated as rounded-at-the-base semi-circles. This shape minimizes the effect of the basal viscous drag, as the contact surface in the direction of the salt flow, which is parallel to the slope, is almost infinitely small. Increasing the aspect ratio of the minibasins and making them wider increases the contact length between the minibasin and the base salt, thus increasing viscous drag and potentially reducing minibasin translation velocity (Figure 10a and Figure SI-5). We test this effect using numerical simulations of minibasins of different aspect ratios and basal lengths, noting small differences in their translation velocities (Figure 10a). Although, the overall effect of increasing minibasin aspect ratio is much less dramatic when compared to the effect of increasing minibasin thickness, it is notable in the case of thick minibasins. If a minibasin is thin and the effect of the base-of-salt is negligible (i.e. the kinematics can still be described by the dashed red curve given by Eq. (4), Figure 9a), the aspect ratio has almost no influence on translation velocity. For example,

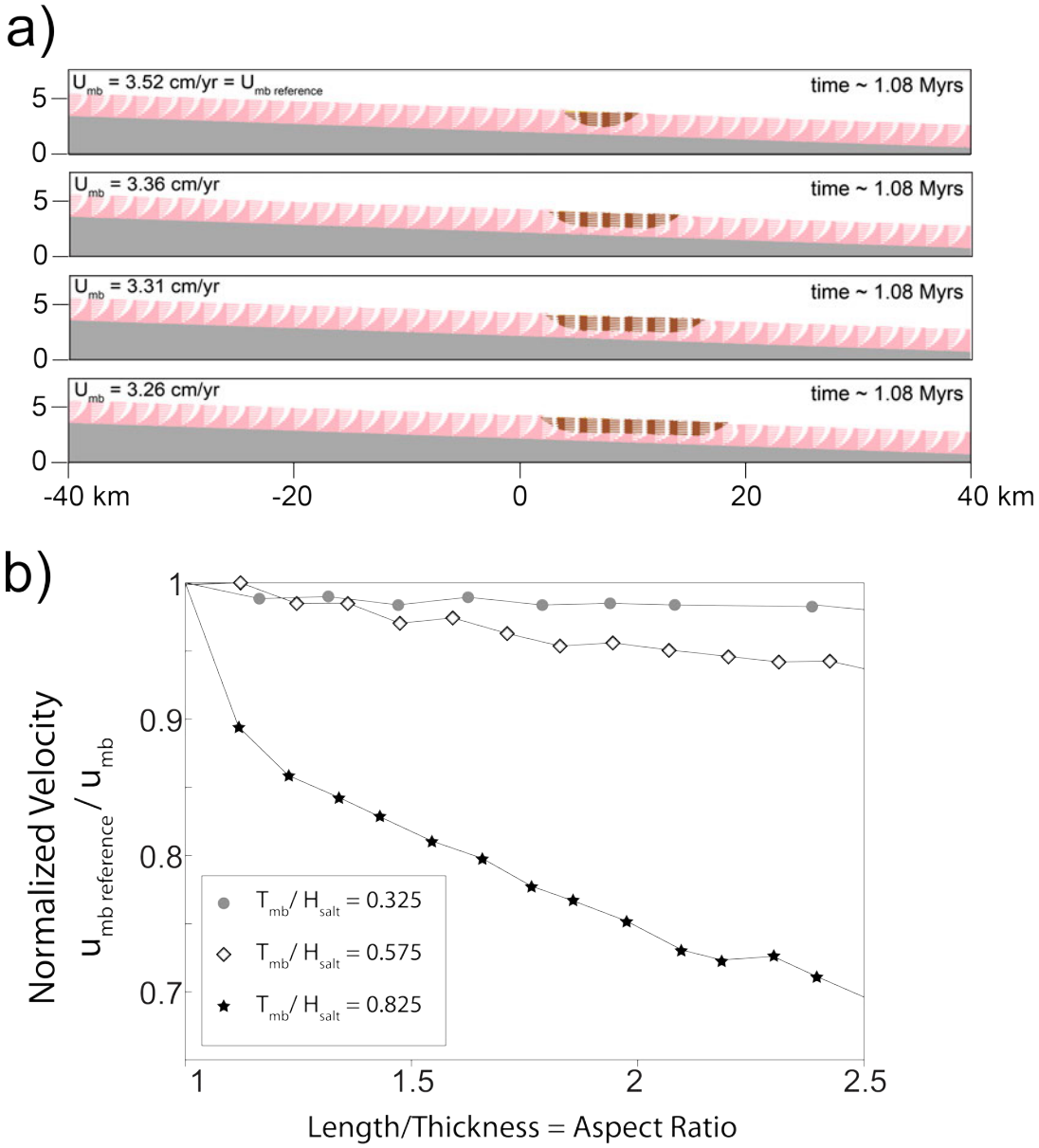

Figure 10 – **a)** Screenshots at the same time-step of four simulations with neutral-density minibasins of same initial thickness but different length or aspect ratio. The minibasin to salt thickness of this example is T_{mb}/H_{salt} ~ 0.575. The arrow indicates the centre of the minibasin, which at the beginning of the simulations was located at the same position for all cases. The arrow at this time step illustrates that although there has been differential translation, the amount is relatively small. The longest minibasin, which has the highest aspect ratio, (lower panel) has the slowest mean velocity of all, although the differences are relatively small. **b)** Graph showing the relation between the aspect ratio and minibasin velocity, for neutral buoyancy minibasins with three different initial thicknesses. Each point is one simulation. Each marker type (start, diamond, circle) corresponds to one thickness (e.g. diamond shaped markers correspond to thicknesses shown in (a)). The velocity is normalized to illustrate a decrease from the reference velocity (given by the minibasin with the smallest aspect ratio. Overall, the higher the aspect ratio is, the lower the translation velocity is. However, as discussed in text, thickest minibasins show a higher effect of the aspect ratio.

a thin minibasin with a thickness to salt thickness ratio of T_{mb}/H_{salt} ~ 0.325, is not influenced by the base-of-salt (Figure 9a, dashed red line). In such a case, increasing the minibasin width to double the original width (factor of 2 increase), results in a < 5% decrease in translation velocity (Figure 10b; line described by grey circles for T_{mb}/H_{salt} ~ 0.325). If instead, the initial minibasin is thick and its velocity is already affected by the base-of-salt as described previously (i.e. deviates from Eq. (4), Figure 10a), then changes in aspect ratio become more significant. For example, for a minibasin with a T_{mb}/H_{salt} of ~ 0.825, increasing minibasin width by a factor of 2 results in a 25% decrease in translation velocity (Figure 10b; line described by black stars for T_{mb}/H_{salt} ~0.825). This effect can be explained by the fact we are increasing the surface of the minibasin exposed to viscous drag.

6 Strain Patterns around Minibasins Moving at Different Velocities

We have shown that neutral-density minibasins of different initial thicknesses translate at different velocities. We have also shown that subsiding minibasins decrease their velocity as they increase their thickness, as well as providing new intra-slope accommodation as they translate downslope. Now we explore how minibasins interact as they translate downslope at different velocities. Can the different translation velocities result in minibasins converging or diverging from each other as they travel downslope? If so, how does this influence local strain patterns?

We can hypothesise that if a minibasin translates faster than another minibasin further upslope of it, then over time, the distance between the two will increase. In contrast, if the upslope minibasin is faster than the downslope minibasin, it follows that the opposite will occur and the minibasins will converge and possibly collide. To test these hypotheses and illustrate the resulting strain patterns around minibasins moving downslope at different velocities, we performed a final series of numerical models comprising a chain of three neutral-density minibasins of different thicknesses (Figure 11a, b, see also Figure SI-6). A thin minibasin located upslope (MB1) moves downslope along with a thick minibasin (MB2) located further downslope, and a third thin minibasin located even further downslope (MB3) (Figure 11a, b). The minibasins are separated by diapirs labelled D1 and D2 in Figure 11a, b. Given this minibasin configuration, we test two scenarios: one in which the diapirs between minibasins contain no roof, and other in which the diapirs between the minibasins are overlain by a 200 m-thick roof of visco-plastic material that is weaker (lower friction angle; ϕ = 15° and lower cohesion; C = 5 MPa) than the minibasins (Figure 11a, b) to allow its deformation.

We first discuss the case with no roof over the diapirs. At the beginning of the simulation, the minibasins translate downslope (Figure 11a). The evolution of the velocity for each of the minibasins is shown in Figure 11c. MB1 and MB3, the thin minibasins, translate faster than MB2, the thick minibasin. Because the thinner minibasins are faster than the thicker one, the furthest downslope minibasin (MB3) diverges from the thick minibasin located just upslope (MB2). Conversely, the upslope minibasin (MB1) converges with the thick minibasin and the intervening diapir is squeezed (Figure 11a). This convergence and divergence between the minibasins can be analysed in terms of strain and strain rate, as calculated by the change in distance between the minibasins and is shown in Figure 12a. Convergence between the minibasins can occur because of the shortening accommodated by squeezing the intervening diapir, whereas the divergence must be accommodated by extension and widening of the intervening diapir. When the diapirs are not capped by a sediment roof, shortening and extension associated with converging and diverging minibasins is cryptically accommodated by the intervening salt. It would be very difficult to detect this deformation in natural systems. Once the minibasins have collided (ca. 0.65 Myr, Figure 11a, c), the shortening strain rate is dramatically reduced. Further shortening between minibasins MB1 and MB2 continues at a lower rate by means of MB1 being thrust over MB2.

In the second scenario, in which the diapirs are covered by a roof and the minibasins are thus physically connected, the roof records the resulting strain patterns (Figure 11b). This is especially true between converging MB1 and MB2 (11d). As the minibasins start translating downslope, the thin minibasins move faster than the intervening thick minibasin. As in the example with no roof, the upslope thin minibasin (MB1) starts to converge with the slower-moving thick minibasin (MB2). In contrast, the downslope thin minibasin (MB3) diverges from the slower-moving upslope minibasin (MB2). The different translation velocities between the minibasins are again accommodated by deformation of the intervening diapirs. However, in this case, the presence of the roof on top of the diapirs results in the development of an additional suite of structures. For example, the roof of diapir D2 stretches and breaks as the thin, faster minibasin MB3 diverges from MB2 (Figure 11b, e). In contrast, the roof of diapir D1 folds to accommodate the shortening resulting from the upslope, relatively fast, thin minibasin (MB1) converging with the thicker, slower-moving minibasin downslope (MB2) (Figure 11b, e). The resulting strain and strain rate evolution of the diapirs with roofs is different to the case where the diapirs lack roofs (Figure 12). Much more strain, at higher strain rates, can be accommodated due to the different translation velocities when the diapirs do not have roofs, and when all the deformation can be cryptically accommodated by the squeezing or stretching of the salt (Figure 12). The evolution of strain and strain rates of intervening diapirs is dependent on the initial slope angle and salt parameters (see also *Hamdani et al.*, 2021). In the case of the diapirs with roofs, strain and strain rate is also strongly dependent on the thickness and mechanical properties of the roof. Here, we have used a relatively weak material to easily allow deformation of the diapir roof. However, if diapir roofs are sufficiently thick or too mechanically strong to accommodate any deformation due to converging or diverging minibasins, the chain of minibasins would likely translate as a single mechanical unit. Different mechanical properties and thickness of the roof would result in different strain and strain rate evolution graphs of the diapirs (see Figure SI-7).

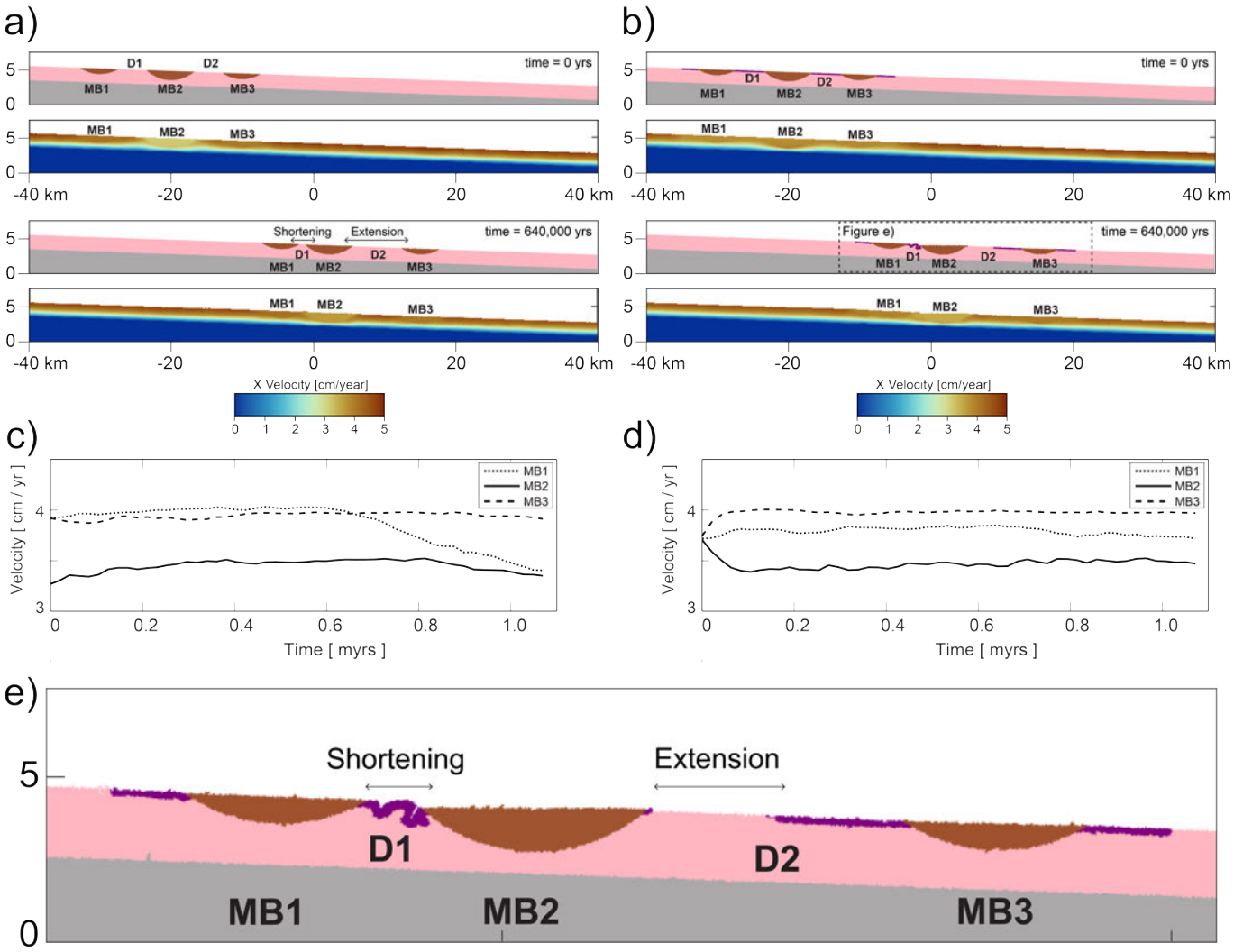

Figure 11 – Screenshots of a two time-step evolution of a chain of three neutral-density minibasins on a slope (from updip to downdip, MB1, MB2 and M3; with intervening diapirs D1 and D2). The minibasin in the centre (MB2) is thicker than the ones updip and downdip. Two scenarios are shown. One scenario in which the diapirs are exposed and not covered by a roof **(a)**, and one in which the diapirs are covered by a weak (see text) roof on top **(b)**. The velocities of the minibasins for each scenario are plotted in **c)** and **d)**. In the simulation with the exposed diapirs (a), as the numerical simulation evolves, the thin minibasins (MB1 and MB3) translate faster than the thick minibasin (MB2) (c). However, as the simulation evolves, updip thin minibasin (MB1), decreases its velocity as it approaches the thick minibasin MB2 (c). In the simulation with covered diapirs (b), because the three minibasins are initially connected by the roof, their starting velocities are the same (d). However, as the simulation evolves, the downdip minibasin (MB3) drifts away from the minibasin in the centre (MB2), the roof in between the two gets stretched (b,d). Instead, the minibasin updip (MB1), converges towards the minibasin in the centre and the roof in between gets shortened by folding (b,c). **e)** Zoomed view of the rectangle of Figure (b) where the deformation of the roof above the diapirs can be observed.

7 Discussion

7.1 Comparison to Natural Examples

We first consider the rates of downslope salt flow in absence of minibasins, for which the Levant Basin provides a good example to test analytical predictions. Based on kinematic indicators, velocity of salt in the Levant Basin has been estimated to be 0.2 cm/yr (*Cartwright et al.*, 2018). Calculations of salt velocity with the analytical equation for scenarios with 0.5 to 1° slope with no minibasins, and salt thickness of 1-1.5 km (i.e., comparable to the Levant Basin) yield values of 0.3-1.3 cm/yr for the maximum and 0.2-0.9 cm/yr for the mean salt velocity, assuming a salt viscosity of 10^{18} Pa s (Eqs. (2) and (3)). As mentioned before, our analytical calculations assume a subaerial slope, and thus they are higher than salt velocities on a water-covered slope. Yet, the calculated values are of a similar order-of-magnitude to local estimates in the Levant Basin. This adds confidence that the analytical solution appears to broadly capture the actual physics occurring in natural examples.

Now, we consider the observed rates at which minibasins translate downslope. In the northern Gulf of Mexico, translation rates of c. 0.6 cm/year are calculated for rafted minibasins and ramp-syncline basins, that moved 40 km downslope from Pliocene

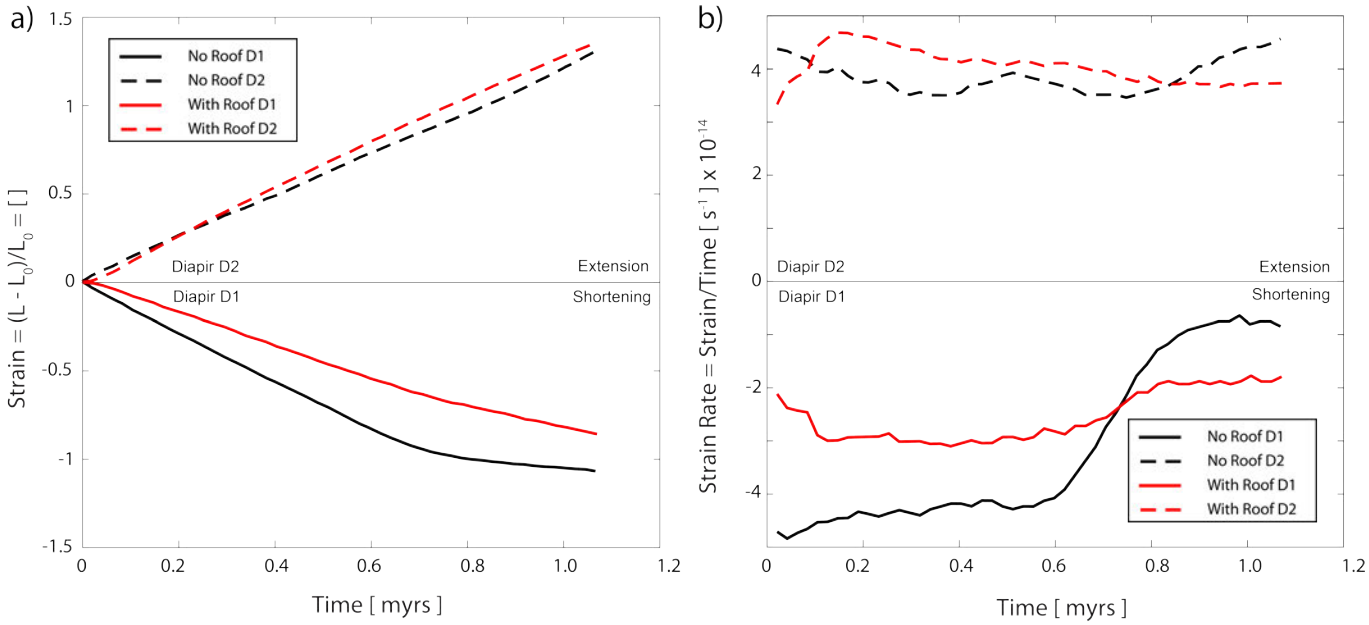

Figure 12 – **a)** Strain accommodated by the diapirs D1 and D2, for the simulations with minibasin arrays and with no roof or with a weak roof. D1 is the diapir located upslope, in between the converging minibasins MB1 and MB2. As such, diapir D1 accommodates the shortening, as shown by the negative value of the strain. The opposite is true for diapir D2, which is located downslope, between diverging minibasins MB2 and MB3. It must also be noted, the higher amount of compressional strain, accommodated by the case in which the diapir has no roof. **b)** Strain rate calculated for the diapirs D1 and D2. The negative value of the strain rate indicates the shortening which is being accommodated by diapir D1. Note how in the case of the diapir with roof, the initial strain rate of the shortened diapir D1, is less than half than the case of diapir without roof (-2e10^{-14} s^{-1}, compared to -5e10^{-14} s^{-1}). The strain rate of shortened diapir roof is dramatically decreased when minibasins collide (after circa 0.65 Myr), after which slower shortening can further be accommodated by minibasin overthrusting. Additionally, in the case of the extended diapir D2, both the cases with roof and no-roof start accommodating the deformation early in their evolution.

to recent (*Fernandez et al.*, 2021). The thickness of the salt canopy over which these depocenters translated was likely between 2 and 3 km (e.g. *Hudec et al.*, 2013). In the Levant Basin, translation rates of 0.2 to 0.3 cm/yr from Pliocene to recent are calculated from ramp-syncline basins in an area where the salt thickness is estimated to be ca. 2 km (*Evans et al.*, 2021). Lower translation velocities, of around 0.03 to 0.05 cm/yr, are proposed for ramp-syncline basins in the Campos Basin, where salt thickness is estimated to be < 1 km (*Pichel et al.*, 2020). There are intrinsic uncertainties related to these velocity estimations in natural examples. For example, velocities obtained from ramp-syncline basins, represent average velocities over a period during which basin thickness gradually increases and may vary through time (e.g. Evans et al., 2021b). In the case of rafted minibasins, the translation mainly occurs over a salt canopy, which can have very rugose base-of-salt topography (e.g. *Fernandez et al.*, 2021). In either case, the thickness of the salt surrounding the minibasin and the effective angle of the slope, at the moment of the minibasin translation, are rarely well-constrained.

Using a very conservative assumption (given local spatial variations) that the slope in all three examples is of 1° degree, we can calculate maximum theoretical salt velocities, i.e., the maximum theoretical salt velocities for a 3, 2 and 1 km thick-salt layer are 5.34, 2.33 and 0.59 cm/year respectively, assuming a salt viscosity of 10^{18} Pa s. These values are one order-of-magnitude higher than the observed translation velocities. However, assuming a higher salt viscosity of 5x10^{18} Pa s, which is well-within the range of values reported for salt (e.g. *Mukherjee et al.*, 2010), the maximum analytical salt velocities are dramatically lower, i.e., 1.07, 0.48 and 0.08 cm/yr respectively. These values are now of similar order-of-magnitude to those observed in the natural examples. In any case, the calculated values are the theoretical upper bounds of the translation velocity, because minibasins and ramp-syncline basins would only be close to that of the theoretical maximum velocity value when they initiate, and are accordingly very thin compared to the total salt thickness. As the minibasins or ramp-syncline basins thickened, their translation velocity would have decreased. For example, once they reached a thickness equivalent to 50% or 70%, of total thickness of salt layer, their translation velocity would have decreased to 83% or 66% of the maximum salt velocity (based on our analytical estimation; Figure 9). Assuming a viscosity of salt of 5x10^{18} Pa s and minibasin thickness of 66% of salt thickness, we get theoretical minibasin translation velocities of 0.70, 0.32 and 0,05 cm/yr, which are even closer to the velocities observed in the natural examples. Thus, observed velocities can be matched by the analytical solution when a higher viscosity of salt is assumed.

7.2 Implications for minibasin kinematics on salt-detached slopes

As salt flows down a slope, minibasins that have developed in the salt layer are also translated. We modelled simple scenarios where the base-of-salt in the slope is smooth. A striking finding from our modelling is that even in the case of a smooth base-of-salt, minibasin translation can still be complex, as minibasins of different thicknesses and geometries can translate at different velocities. Furthermore, minibasin translation can decrease dramatically as the salt beneath them thins ahead of welding (e.g. *Krueger*, 2010; *Wagner and Jackson*, 2011). The observations from the numerical models are synthesized in Figures 13a and b, which shows how minibasin thickness, width and density influence minibasin velocity. Minibasins translating at different velocities can converge or diverge, and hence modify strain patterns around them (Figures 11 and 12). Shortening is accommodated in between two converging minibasins, while extension occurs in between two diverging minibasins (Figure 13c). This localized shortening and extensional strains can be cryptic if the salt lacks a roof, with minibasin spacing erroneously interpreted as being an original feature.

The base-of-salt in natural salt basins can, however, be highly rugose and have considerable relief (Figure 1c). When minibasins translate downslope over a rugose base-of-salt, if thick enough, the minibasin can weld at its base, or buttress against a high-relief base-salt feature, obstructing the minibasin from further downslope translation (e.g *Krueger*, 2010; *Wagner and Jackson*, 2011; *Duffy et al.*, 2020). The complex deformation patterns that result from different degrees of minibasin obstruction at both the minibasin-scale and the sub-regional scale have been recently described in detail in an area where the base-of-salt has very high relief (i.e. the northern Gulf of Mexico canopy; *Duffy et al.*, 2020; *Fernandez et al.*, 2019). Minibasin obstruction results in shortening immediately upslope of the obstructed minibasin, and extension on the downslope side of the obstructed minibasin (e.g. *Duffy et al.*, 2020). The interactions between minibasins and the base-of-salt and the potential for minibasins to be obstructed, is important when trying to understand strain patterns around minibasins.

Depending on the initial configuration of minibasins translating at different velocities over a smooth base-of-salt slope, strain patterns can be similar to those described near obstructed minibasins (*Duffy et al.*, 2020), which are generally characterised by up-dip shortening and down-dip extension (Figure 13c). Thus, when attempting to understand strain patterns and minibasin kinematics on salt-detached slopes (see for example Figure 1c), it is important to consider the influence of one, or a combination of: i) minibasin obstruction and interaction with the base-of-salt (sensu *Duffy et al.*, 2020); and ii) kinematic interactions between minibasins translating at different velocities in the absence of base-of-salt relief (this study). Assessing whether convergence between minibasins occurred before primary welding and obstruction may be a challenging task if the relative timing of deformation events cannot be constrained. The seismic cross section in Figure 1c, shows an array of minibasins with a thick minibasin that is welded to the base-of-salt in the centre. The diapirs upslope of this welded minibasin have been shortened, as indicated by a secondary weld and folding of the diapir roofs, thus at first glance, the configuration and deformation patterns appear to reflect minibasin obstruction (i.e. shortened diapir immediately upslope of a primary welded minibasin). However, prior to the thick minibasin welding to the base-of-salt, these minibasins were most probably located further upslope from their present position. In fact, the two minibasins upslope of the thicker and presently primary welded minibasin are noticeably thinner. Given this, it is possible that the shortened diapirs are simply the result of differential minibasin translation velocities related to minibasin thickness (as outlined in this study), rather than as a result of primary welding (sensu *Krueger*, 2010; *Duffy et al.*, 2020; *Fernandez et al.*, 2019).

7.3 Limitations of the Modelling Approach

The comparison to natural examples has illustrated that it is not always possible to constrain the parameters of the analytical solution with observations. This is especially true for the salt viscosity. In fact, the rheology of salt at geological time-scales is a matter of debate, and both linear and non-linear rheologies have been proposed for different combinations of strain rates and differential stresses (e.g. *Urai et al.*, 2008). In our models, we have assumed salt to be linear viscous with a viscosity of 10^{18} Pa s, a value commonly assumed for salt-rock (e.g. *Mukherjee et al.*, 2010). In natural examples however, evaporite layers are rarely composed of pure salt-rock (halite), and the presence of non-halite lithologies within layered evaporite sequences will impact the viscosity of the sequence, making it effectively weaker or stronger (e.g. *Jackson and Hudec*, 2017).

Other assumptions made in our modelling approach to facilitate the comparison to the simple 1D analytical solution are that the thickness of the salt layer and the angle of the slope do not change through time. It is expected that during the regional evolution of a continental margin and as new minibasins are being formed on top of the downslope flowing salt, both the slope angle (e.g. inherited base-of-salt relief, margin tilting due to thermal and isostatic effects) and salt thickness (e.g. accumulation of salt at the base of the continental slope, draining of salt at the upper part of the slope) could dynamically change through time and space. Such dynamic changes would only be captured in

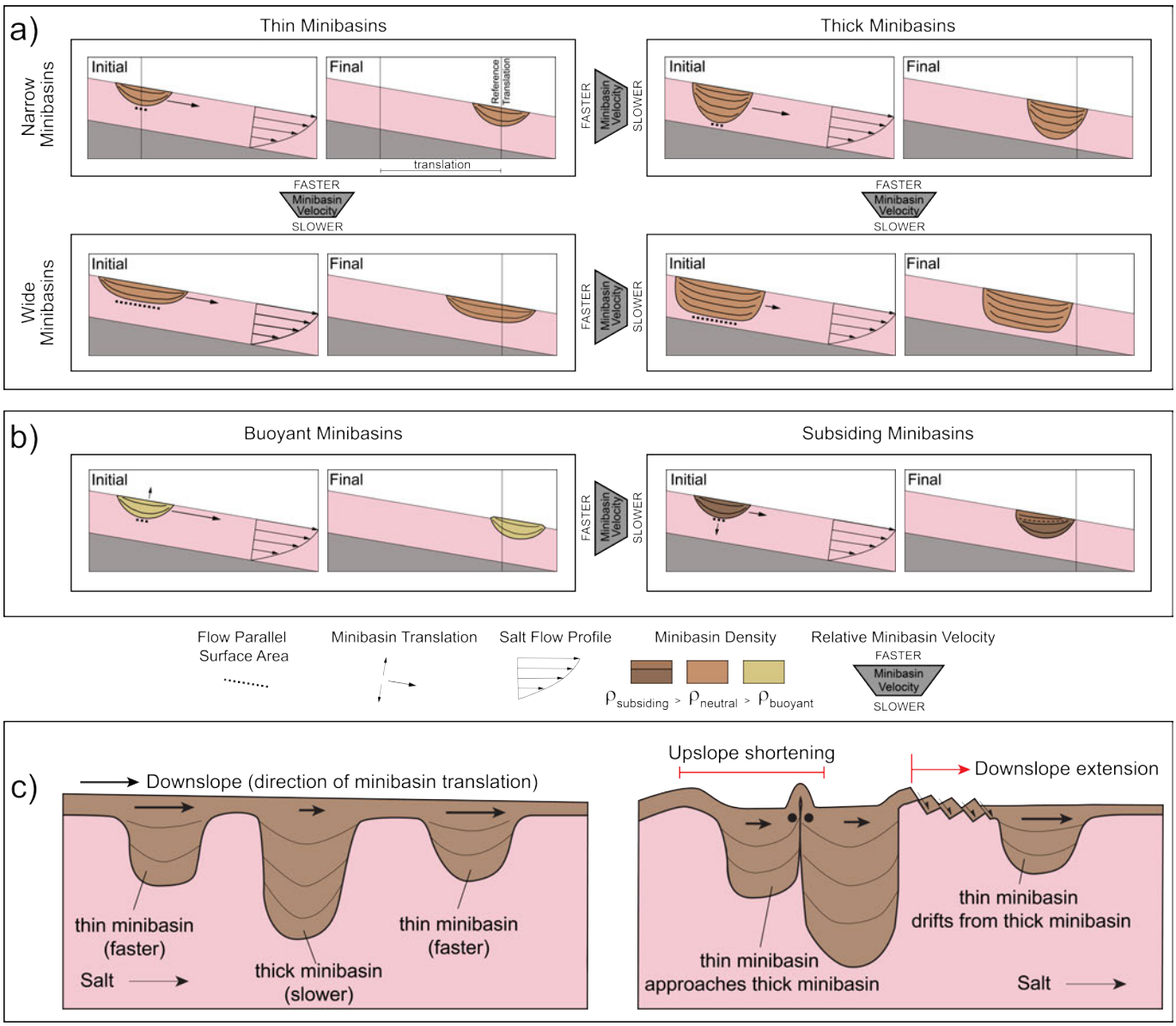

Figure 13 – Conceptual sketches reviewing the main controls on minibasin velocity in the numerical simulations with neutral-density minibasins (a) and buoyant and subsiding minibasins (b). **a)** The main control on minibasin velocity in the case of neutral-density minibasins is the minibasin thickness (or distance to base-of-salt). Thicker minibasins have a lower translation velocity and thus will cover less translation distance for the given time, when compared to thinner minibasins. For a minibasin of a given thickness, its width (measured as an aspect ratio, width to thickness) also influences the translation velocity. A wider minibasin translates slower than a narrow one. The velocity decrease due to higher flow parallel surface area, is even more dramatic in the case of thick minibasins. **b)** Minibasins that are either buoyant or subsiding will change the distance from the base-of-salt as they translate. Subsiding minibasins create accommodation space for new sediments and increase their thickness, thus reducing their distance from the base of the salt, and ultimately reducing their translation velocity. **c)** Sketch illustrating that minibasins translating at different velocities can result at similar strain patterns of updip shortening and downdip extension without minibasin obstruction.

a margin-scale numerical modelling approach (e.g. *Pichel et al.*, 2022), where the effect of additional processes and parameters on minibasin translation velocity could be assessed.

The key finding of this work is that coexisting minibasins can translate downslope at different velocities and that this can impact strain patterns around them. This has been demonstrated in 2D with an analytical solution and numerical models. However, salt flow is three-dimensional. We speculate that in the case of isolated minibasins in 3D, the fundamental principles outlined in this study would still apply, notably in terms of how the minibasin velocity relates to the overall theoretical salt velocity profile. The isolated minibasins will translate at a slower velocity than the maximum salt velocity (at the salt surface). In 3D, however, increasing minibasin thickness, length (along slope direction) or width (along strike direction), will increase the surface area exposed to viscous drag, more than it would proportionally in 2D.

The implications of considering the three-dimensional behaviour of minibasins extend beyond simple consideration of their velocity, given

it may also influence minibasin kinematics and strain patterns. For example, different translation velocities are also possible between neighbouring minibasins that are not necessarily located directly upslope or downslope of one another (i.e. as in our numerical simulations). Where minibasins are slightly offset from the downslope pathway of neighbouring minibasins, additional strike-slip components will be added to the zones of shortening (transpression) and extension (transtension). The complex three-dimensional strains due to differential translation of the sedimentary cover are described using seismic reflection data imaging natural systems (e.g. *Krueger*, 2010; *Duffy et al.*, 2020; *Fernandez et al.*, 2019), and are predicted by physical models (*Dooley et al.*, 2019; *Duffy et al.*, 2020). In those previous works, strike-slip patterns around minibasins are discussed within the context of minibasins becoming variably obstructed due to welding. However, we emphasise here that different translation velocities between minibasins may be an important contributor to such complex strains, irrespective of whether a minibasin welds and stops.

8 Summary and Conclusions

Due to the viscous behaviour of salt over geologic time and the effect of gravity, a layer of salt lying over an inclined plane flows downslope. Assuming that the thickness of the salt layer is kept constant, the velocity of the flowing salt can be described by a mathematical expression. Such an analytical expression predicts a velocity profile with a maximum salt velocity at the top of the salt layer (salt topography), decreasing to zero at the base of the salt layer. We have reproduced the predictions of the analytical solution for salt flow with 2D numerical simulations of a salt layer overlying an inclined plane.

Returning to our initial question of how fast can minibasins translate on a slope, the answer is that it depends on a number of factors. At a first order approach, the comparison of our numerical simulations with the analytical solution show that minibasins travel at a slower velocity than the theoretical maximum salt velocity (Figure 9). On top of that, there are a number of factors to consider that will affect minibasin velocity (summarized in Figure 13a).

Minibasin thickness is the main factor controlling minibasin velocity. If far enough from the base-of-salt, minibasin velocity is proportional to the velocity of the uppermost salt sublayer of equivalent thickness and it can be calculated with a simple 1D analytical solution of a salt layer flowing over an inclined plane. Thicker minibasins translate slower than thinner minibasins. Furthermore, when the base of the minibasins is close to the base of the salt, the velocity is further decreased, and the velocity cannot be calculated with the same 1D analytical solution. This is true for all minibasins regardless of their density or shape.

In the case of neutral-density minibasins, their thickness remains constant during their translation, and so does their translation velocity. If minibasins are of non-neutral-density, whether they be subsiding or rising, their salt-embedded thicknesses change during their translation, and so does their velocity. Minibasins that are denser than salt subside into salt as they translate, and if new sediments are deposited, their thickness increases. As the thickness of subsiding minibasins increases, their translation velocity decreases through time. Regardless of the density structure of a minibasin, their velocity can be predicted analytically, as long as they are far enough from the base of salt (minibasin thickness is less than 70% of the salt thickness) (Eq. (4), Figure 9a, b).

When the minibasin is thick enough so that it is close to the base of salt, minibasin velocity decreases more dramatically than as predicted by Eq. (4) (Figure 9a, b). For such cases, the shape or aspect ratio of the minibasin is another factor to be considered. The aspect ratio of minibasins controls the area or length of the minibasin contact surface at the direction parallel to salt flow exposed to viscous drag. Longer minibasins have more contact surface. The longer the contact surface, the greater the effect of viscous drag at the base of the minibasin is, and therefore, the more the minibasin velocity is reduced (Figure 10).

The findings from our numerical modelling approach have direct and significant implications for understanding minibasin behaviour, kinematics and strain patterns on natural salt-detached slopes. Minibasins of different maturities, and thus differing thicknesses and density structures, can coexist at any given time in the translational domain of a salt-detached continental slope (e.g. *Ge et al.*, 2021). Our study shows that such differences will result in minibasins translating downslope at different velocities. Depending on the initial configuration of the minibasins, this may result in convergence and divergence of minibasins, and minibasins will be able to translate past another in a three-dimensional configuration. These minibasin kinematics will result in deformation being accommodated by the intervening salt structures (e.g. diapirs), or by the overlying sedimentary cover (e.g. diapir roof). When interpreting strain patterns around minibasins, it is important to consider that shortening and extensional deformation can be the result of minibasins translating at different velocities in continental slopes.

Acknowledgements

Colour schemes used are from Crameri (2021). Thanks to WesternGeco for providing permission to show the 2D seismic section. The project was funded by the Applied Geodynamics Laboratory (AGL) Industrial Associates program (for an updated list of sponsors check http://www.beg.utexas.edu/agl/sponsors). The

authors received additional support from the Jackson School of Geosciences, The University of Texas at Austin. We thank Antonio Teixell for his comments on an earlier version of the manuscript. We also thank the reviewers Attila Balazs, Conor O'Sullivan, and Dan Tamas, whose comments helped improve the manuscript. Finally, we would like to thank the editors of Tektonika for the handling of the manuscript.

Author contributions

NF designed the study, performed the simulations, analyzed the results and wrote the manuscript. **OBD**, **CALJ**, **BJK**, **TD** and **MH** contributed to the interpretation of the results and to the writing and editing of the manuscript.

Data availability

The simulations shown in this study were performed with the numerical code MVEP2. MVEP2 is public and available from https://bitbucket.org/bkaus/mvep2/. The version of MVEP2 used for this study corresponds to the commit ID number [48165b4].

Competing interests

The authors declare that they have no competing interests.

Peer review

This publication was peer-reviewed by Attila Balazs, Conor O'Sullivan, Dan Tamas. The full peer-review report can be found here: tektonika.online/index.php/home/article/view/22/59

Copyright notice

References

Aftabi, P., M. Roustaie, G. I. Alsop, and C. J. Talbot (2010), InSAR mapping and modelling of an active iranian salt extrusion, *Journal of the Geological Society*, *167*(1), 155–170, doi: 10.1144/0016-76492008-165.

Brun, J.-P., and X. Fort (2011), Salt tectonics at passive margins: Geology versus models, *Marine and Petroleum Geology*, *28*(6), 1123–1145, doi: 10.1016/j.marpetgeo.2011.03.004.

Brun, J.-P., and X. Fort (2012), Salt tectonics at passive margins: Geology versus models – reply, *Marine and Petroleum Geology*, *37*(1), 195–208, doi: 10.1016/j.marpetgeo.2012.04.008.

Brun, J.-P., and O. Merle (1985), Strain patterns in models of spreading-gliding nappes, *Tectonics*, *4*(7), 705–719, doi: 10.1029/TC004i007p00705.

Cartwright, J., C. Kirkham, C. Bertoni, N. Hodgson, and K. Rodriguez (2018), Direct calibration of salt sheet kinematics during gravity-driven deformation, *Geology*, *46*(7), 623–626, doi: 10.1130/g40219.1.

Dabrowski, M., M. Krotkiewski, and D. W. Schmid (2008), MILAMIN: MATLAB-based finite element method solver for large problems, *Geochemistry, Geophysics, Geosystems*, *9*(4), doi: 10.1029/2007GC001719.

De Jong, K. A., and R. Scholten (1973), *Gravity and tectonics*, Wiley.

Diegel, F. A., J. F. Karlo, D. C. Schuster, R. C. Shoup, P. R. Tauvers, M. P. A. Jackson, D. G. Roberts, and S. Snelson (1995), Cenozoic structural evolution and Tectono-Stratigraphic framework of the northern gulf coast continental margin, in *Salt Tectonics: A Global Perspective*, vol. 65, p. 0, American Association of Petroleum Geologists, doi: 10.1306/m65604c6.

Dooley, T., O. Duffy, M. Hudec, and N. Fernandez (2019), PS shortening of diapir provinces: Translation, tilting and rotation of minibasins in isolated minibasin systems, in *AAPG Annual Convention and Exhibition*.

Duffy, O. B., N. Fernandez, F. J. Peel, M. R. Hudec, T. P. Dooley, and C. A.-L. Jackson (2020), Obstructed minibasins on a salt-detached slope: An example from above the sigsbee canopy, northern gulf of mexico, *Basin Research*, *32*(3), 505–524, doi: 10.1111/bre.12380.

Evans, S. L., and C. A.-L. Jackson (2021), Intra-salt structure and strain partitioning in layered evaporites: implications for drilling through messinian salt in the eastern mediterranean, *Petroleum Geoscience*, *27*(4), doi: 10.1144/petgeo2020-072.

Evans, S. L., C. A.-L. Jackson, and D. Oppo (2021), Taking the pulse of Salt-Detached gravity gliding in the eastern mediterranean, *Tectonics*, *40*(7), e2020TC006,476, doi: 10.1029/2020TC006476.

Fernandez, N., M. R. Hudec, C. A.-L. Jackson, T. P. Dooley, and O. B. Duffy (2019), The competition for salt and kinematic interactions between minibasins during density-driven subsidence: observations from numerical models, *Petroleum Geoscience*, *26*(1), 3–15, doi: 10.1144/petgeo2019-051.

Fernandez, N., O. B. Duffy, F. J. Peel, and M. R. Hudec (2021), Influence of minibasin obstruction on canopy dynamics in the northern gulf of mexico, *Basin Research*, *33*(1), 427–446, doi: 10.1111/bre.12480.

Fiduk, J. C. (2014), Origin, transportation, and deformation of mesozoic carbonate rafts in the northern gulf of mexico, *The Houston Geological Society Bulletin*, *57*(2), 25–27.

Ge, Z., M. Warsitzka, M. Rosenau, and R. L. Gawthorpe (2019a), Progressive tilting of salt-bearing continental margins controls thin-skinned deformation, *Geology*, *47*(12), 1122–1126, doi: 10.1130/g46485.1.

Ge, Z., M. Rosenau, M. Warsitzka, and R. L. Gawthorpe (2019b), Overprinting translational domains in passive margin salt basins: insights from analogue modelling, *Solid Earth*, *10*(4), 1283–1300, doi: 10.5194/se-10-1283-2019.

Ge, Z., R. L. Gawthorpe, L. Zijerveld, and A. P. Oluboyo (2021), Spatial and temporal variations in minibasin geometry and evolution in salt tectonic provinces: Lower

congo basin, offshore angola, *Basin Research*, *33*(1), 594–611, doi: 10.1111/bre.12486.

Gevantman, L. H., and J. Lorenz (1981), *Physical properties data for rock salt*, vol. 167, US Department of Commerce, National Bureau of Standards.

Ghassemi, M. R., and M. Roustaei (2021), Salt extrusion kinematics: insights from existing data, morphology and InSAR modelling of the active emergent anguru diapir in the zagros fold and thrust belt, iran, *Journal of the Geological Society*, *178*(6), doi: 10.1144/jgs2020-136.

Granado, P., J. B. Ruh, P. Santolaria, P. Strauss, and J. A. Muñoz (2021), Stretching and contraction of extensional basins with Pre-Rift salt: A numerical modeling approach, *Frontiers of Earth Science in China*, *9*, doi: 10.3389/feart.2021.648937.

Hamdani, I., E. Aharonov, J.-A. Olive, S. Parez, and Z. Gvirtzman (2021), Initiating salt tectonics by tilting: Viscous coupling between a tilted salt layer and overlying brittle sediment, *Journal of Geophysical Research, [Solid Earth]*, *126*(7), e2020JB021,503, doi: 10.1029/2020JB021503.

Hudec, M. R., M. P. A. Jackson, and F. J. Peel (2013), Influence of deep louann structure on the evolution of the northern gulf of mexico, *AAPG Bulletin*, *97*(10), 1711–1735, doi: 10.1306/04011312074.

Jackson, M. P. A., and M. R. Hudec (2005), Stratigraphic record of translation down ramps in a passive-margin salt detachment, *Journal of Structural Geology*, *27*(5), 889–911, doi: 10.1016/j.jsg.2005.01.010.

Jackson, M. P. A., and M. R. Hudec (2017), *Salt Tectonics: Principles and Practice*, Cambridge University Press, Cambridge, doi: 10.1017/9781139003988.

Jackson, M. P. A., and C. J. Talbot (1991), A glossary of salt tectonics, *Tech. rep.*, Bureau of Economic Geology, doi: 10.23867/gc9104D.

Jackson, M. P. A., M. R. Hudec, and T. P. Dooley (2010), Some emerging concepts in salt tectonics in the deepwater gulf of mexico: intrusive plumes, canopy-margin thrusts, minibasin triggers and allochthonous fragments, in *Petroleum Geology: From Mature Basins to New Frontiers – Proceedings of the 7th Petroleum Geology Conference*, vol. 7, edited by B. A. Vining and S. C. Pickering, p. 0, Geological Society of London, doi: 10.1144/0070899.

Johnson, T. E., M. Brown, B. J. P. Kaus, and J. A. VanTongeren (2014), Delamination and recycling of archaean crust caused by gravitational instabilities, *Nature geoscience*, *7*(1), 47–52, doi: 10.1038/ngeo2019.

Kaus, B. J. P. (2010), Factors that control the angle of shear bands in geodynamic numerical models of brittle deformation, *Tectonophysics*, *484*(1), 36–47, doi: 10.1016/j.tecto.2009.08.042.

Kent, P. E. (1958), Recent studies of south persian salt plugs1, *AAPG Bulletin*, *42*(12), 2951–2972, doi: 10.1306/0bda5c2d-16bd-11d7-8645000102c1865d.

Krueger, S. W. (2010), Dynamics of tear faults in the salt-detached systems of the northern gulf of mexico, *Tulsa, OK: American Association of Petroleum Geologists Search and Discovery*.

Lees, G. M. (1927), Salzgletscher in persien, *Mitt geol Ges Wien*, *22*, 29–34.

Li, S., S. Abe, J. L. Urai, F. Strozyk, P. A. Kukla, H. Van Gent, P. Berest, M. Ghoreychi, F. Hadj-Hassen, and M. Tijani (2012), A method to evaluate long-term rheology of zechstein salt in the tertiary, *Proc. Mech. Beh. Salt VII*, pp. 215–220.

Marton, G. L., G. C. Tari, and C. T. Lehmann (2000), Evolution of the angolan passive margin, west africa, with emphasis on Post-Salt structural styles, in *Atlantic Rifts and Continental Margins*, pp. 129–149, the American Geophysical Union, doi: 10.1029/GM115p0129.

Mohammadnia, M., M. Najafi, and Z. Mousavi (2021), InSAR constraints on the active deformation of salt diapirs in the kalut basin, central iran, *Tectonophysics*, *810*, 228,860, doi: 10.1016/j.tecto.2021.228860.

Mukherjee, S., C. J. Talbot, and H. A. Koyi (2010), Viscosity estimates of salt in the hormuz and namakdan salt diapirs, persian gulf, *Geological magazine*, *147*(4), 497–507, doi: 10.1017/S001675680999077X.

Peel, F. J. (2014), The engines of gravity-driven movement on passive margins: Quantifying the relative contribution of spreading vs. gravity sliding mechanisms, *Tectonophysics*, *633*, 126–142, doi: 10.1016/j.tecto.2014.06.023.

Peel, F. J., C. J. Travis, J. R. Hossack, M. P. A. Jackson, D. G. Roberts, and S. Snelson (1995), Genetic structural provinces and salt tectonics of the cenozoic offshore U.S. gulf of mexico: A preliminary analysis, in *Salt Tectonics: A Global Perspective*, vol. 65, p. 0, American Association of Petroleum Geologists, doi: 10.1306/m65604c7.

Pichel, L. M., F. Peel, C. A. L. Jackson, and M. Huuse (2018), Geometry and kinematics of salt-detached ramp syncline basins, *Journal of Structural Geology*, *115*, 208–230, doi: 10.1016/j.jsg.2018.07.016.

Pichel, L. M., C. A.-L. Jackson, F. Peel, and T. P. Dooley (2020), Base-salt relief controls salt-tectonic structural style, são paulo plateau, santos basin, brazil, *Basin Research*, *32*(3), 453–484, doi: 10.1111/bre.12375.

Pichel, L. M., R. S. Huismans, R. Gawthorpe, J. I. Faleide, and T. Theunissen (2022), Coupling Crustal-Scale rift architecture with passive margin salt tectonics: A geodynamic modeling approach, *Journal of Geophysical Research, [Solid Earth]*, *127*(11), e2022JB025,177, doi: 10.1029/2022JB025177.

Pilcher, R. S., R. T. Murphy, and J. McDonough Ciosek (2014), Jurassic raft tectonics in the northeastern gulf of mexico, *Interpretation*, *2*(4), SM39–SM55, doi: 10.1190/int-2014-0058.1.

Ramberg, H. (1981), *Gravity, deformation and the earth's crust: in theory, experiments, and geological application*, Academic Press.

Rowan, M. G., F. J. Peel, and B. C. Vendeville (2004), Gravity-driven fold belts on passive margins, in *Thrust tectonics and hydrocarbon systems*, *AAPG Memoir*, vol. 82, pp. 157–182, American Association of Petroleum Geologists.

Schultz-Ela, D. D. (2001), Excursus on gravity gliding and gravity spreading, *Journal of Structural Geology*, *23*(5), 725–731, doi: 10.1016/S0191-8141(01)00004-9.

Schuster, D. C., M. P. A. Jackson, D. G. Roberts, and S. Snelson (1995), Deformation of allochthonous salt and evolution of related Salt-Structural systems, eastern louisiana gulf coast, in *Salt Tectonics: A Global Perspective*, vol. 65, p. 0, American Association of Petroleum Geologists, doi: 10.1306/m65604c8.

Talbot, C. J., and R. J. Jarvis (1984), Age, budget and dynamics of an active salt extrusion in iran, *Journal of Structural Geology*, *6*(5), 521–533, doi:

10.1016/0191-8141(84)90062-2.

Talbot, C. J., and E. A. Rogers (1980), Seasonal movements in a salt glacier in iran, *Science*, *208*(4442), 395–397, doi: 10.1126/science.208.4442.395.

Talbot, C. J., S. Medvedev, M. Alavi, H. Shahrivar, E. Heidari, B. C. Vendeville, Y. Mart, and J.-L. Vigneresse (2000), Salt extrusion at Kuh-e-Jahani, iran, from june 1994 to november 1997, in *Salt, Shale and Igneous Diapirs in and around Europe*, vol. 174, p. 0, Geological Society of London, doi: 10.1144/gsl.Sp.1999.174.01.06.

Tauvers, P. R. (1993), Salt geometry and kinematics, Texas/Louisiana lower slope, northwest gulf of mexico basin. in salt, sediment and hydrocarbons, in *Salt, Sediment and Hydrocarbons*, vol. 16, p. 0, SEPM Society for Sedimentary Geology, doi: 10.5724/gcs.95.16.0271.

Thielmann, M., and B. J. P. Kaus (2012), Shear heating induced lithospheric-scale localization: Does it result in subduction?, *Earth and planetary science letters*, *359-360*, 1–13, doi: 10.1016/j.epsl.2012.10.002.

Turcotte, D. L., and G. Schubert (2002), *Geodynamics*, 2 ed., Cambridge University Press, Cambridge, doi: 10.1017/CBO9780511807442.

Urai, J. L., Z. Schléder, C. J. Spiers, and P. A. Kukla (2008), Flow and transport properties of salt rocks, *Dynamics of complex intracontinental basins: The central European basin system*, pp. 277–290.

Wagner, B. H., and M. P. A. Jackson (2011), Viscous flow during salt welding, *Tectonophysics*, *510*(3), 309–326, doi: 10.1016/j.tecto.2011.07.012.

Wenkert, D. D. (1979), The flow of salt glaciers, *Geophysical research letters*, *6*(6), 523–526, doi: 10.1029/GL006i006p00523.

Zhang, S., Q. Jiang, C. Shi, X. Xu, Y. Gong, J. Xi, W. Liu, and B. Liu (2021), Application of sentinel-1 and-2 images in measuring the deformation of Kuh-e-Namak (dashti) namakier, iran, *Remote Sensing*, *13*(4), 785.